Design considerations to improving sensitivity in SuperSpec: an onchip KID-based, mm-wave spectrometer

Thesis by

Corwin Shiu

In Partial Fulfillment of the Requirements

for the Degree of

Bachelor of Science

California Institute of Technology

Pasadena, California

2015

(Submitted May 15, 2015)

Contents

List of Figures

Acknowledgments

I want to thank Professor Jonas Zmuidzinas for giving my the opportunity to work under his lab. Over the two years I have been involved in his lab, I have not only learned a tremedous amount but have also developed a passion for detector design. I also want to thank Dr. Matt Bradford. Matt has been instrumental to my time here, from bringing me into this lab to overseeing this entire project. Matt provided a tremedous amount of support and this thesis would not have been possible without the guidance and direction he provided.

When I joined this lab, I knew nothing about solid state physics, low temperature detectors, high frequency circuits, astro instrumentation or basically anything that would have made me useful. I've had a ton of help at every stage of this project. Dr. Steve Hailey-Dunshealth has taught me everything I know about instrumentation and taking careful measurements of our detectors. Steve was always avalible whenever I had questions and helped me make sense of a lot of the underlying physics behind the simulation work here. Professor Erik Shirokoff taught me how to use E&M simulation tools for detector design. Erik has provided critical feedback to my simulations and incredibly helpful discussion with everything design related.

Abstract

SuperSpec is an ultra-compact on-chip spectrometer for mm/submm astronomy. SuperSpec's compact size and wide spectral bandwidth will be uniquely powerful to perform multi-object spectroscopy for high redshift surveys, and for tomographic studies of the epoch of reionization (EoR). SuperSpec employs the use of kinetic inductance detectors (KID) to build highly multiplexed arrays. A full instrument of $\sim$ 500 channels can be lithographed on a few cm^2 of silicon.

In this thesis, we explored electromagnetic designs to improve sensitivity of KIDs. We show that we can reliably remove up to 75% of the current design's inductor volume to obtain improvements in sensitivities up a factor of four. We also explored two filter designs that can deliver higher power to the detectors. Our half-wave transmission line filters can only deliver up to 50% of power to the detectors. Both ring resonators and backshorted detectors can deliver unity power, however we found that the large coupling length needed in order to properly use ring resonators would be impractical in a filterbank. Lastly we explored different filterbank designs. Multiple detectors read out together in a single channel has higher resolving power than single detector channels. Backshorted detectors offer higher resolving power than two paired detector channels, but under-performs three or more paired detector channels.

Chapter 1

Background

1.1 Scientific Motivation

Submillimeter/millimeter bands contain rich information in key processes in astronomy and astrophysics. Majority of the radiation energy in the universe is contained in this band. This band is home to many sources, including the Cosmic Microwave Background (CMB), cool molecular clouds responsible for planetary and star formation, and the tails of the far-infrared background (FIB).

It is essential to observe in the far-IR and submm in order to understand galaxy evolution and formation. The most luminous galaxies emit 90% of their energy in the far-IR caused by active star-forming regions warming up dust. At high-redshifts these peaks become redshifted into the submm bands. New observing capabilities are needed to answer fundamental questions in how galaxies evolve. Spectral information of dusty galaxies would give key insight to infer processes about star-formation in galaxies, active galaxatic nuclei, black hole growth and the birth of galaxies.

Closer to home, observing in the mm/submm would give key insight in star and planetary formation. Stars condense from inside thick interstellar clouds. While the chemical processes emit UV and optical light, these photons are obscured and absorbed by the surrounding dust. This energy is emitted at longer wavelengths, in the form of millimeter/submillimeter and infrared light, which is not attenuated by dust absorption. Observing rotational lines of CO and fine structure transitions provide probes deep into molecular clouds and can help answer fundamental questions in both the kinematics and energy balance of clouds.

In addition, millimeter and submillimeter wavelengths contain key information to understanding formation of large scale structure in the early universe. The earliest stars were responsible for the epoch of re-ionization. The very first stars were very massive and emitted in the UV. The ionization radiation would knock electrons off surrounding hydrogen gas and heat the surrounding interstellar medium through photoelectric heating. The gas cools by radiative decay. An important cooling process emits a bright C^+ line

(158 um). By resolving the redshifted C^+ line, we can understand evolution of the ionized gas bubble and the structure of the universe when galaxies just began to form [5].

Spectroscopy remains to be a bottle neck in mm/submm astronomy. Enabling high resolution spectroscopy to study high red-shift galaxies and star formation would require tens of thousands of detectors with NEP on the order of $10^{-18}W/\sqrt{Hz}$. While transition edge senors (TES) bolometers have reached these sensitivity levels, there is no easy path to the number of pixels.

SuperSpec aims to address these problems and enable wide-field, wide-band spectroscopy. Such an instrument would be a powerful tool in multi-object spectroscopy to study early galaxy formation and for tomographic mapping to probe reionization.

1.2 Kinetic Inductance Detectors

1.2.1 Superconducting Electrodynamics

Kinetic Inductance Detectors (KIDs) offer a reliable approach to building large detector arrays. KIDs are pair-breaking detectors and rely on high Q, thin-film superconducting microresonators [3]. Kinetic inductance can be understood intuitively through a classical picture. Cooper pairs are the charge carriers inside of a superconductor. Motion of Cooper pairs carries kinetic energy, and the momentum of these Cooper pairs resists changes in the electric field. This inertia gives rise to the imaginary part of the complex conductivity of the film $\sigma(\omega) = \sigma_1(\omega) - i\sigma_2(\omega)$, which can be interpreted this an additional inductance caused by the supercurrent, hence the name kinetic inductance [11].

Incident radiation with energy above the superconducting gap $h\nu \geq 2\Delta$ breaks Cooper pairs into quasiparticles (electrons). Electrons do not carry a supercurrent and the breaking of Cooper pairs will perturb the complex conductivity $\delta\sigma$ of the film. The electron than rattles around inside the film until it meets another electron and recombines into a Cooper pair, releasing a phonon with energy equal to the superconducting gap. The perturbation in conductivity is described by the Mattis-Bardeen equations [4].

Kinetic inductance detectors are formed by connecting a lossy meander to an interdigitated capacitor (IDC) creating a resonant structure with frequency $\omega^2 = 1/LC$. Incident power breaks Cooper pairs and causes a perturbation in the film's kinetic inductance, which can be precisely tracked as a shift in the resonant frequency of the system.

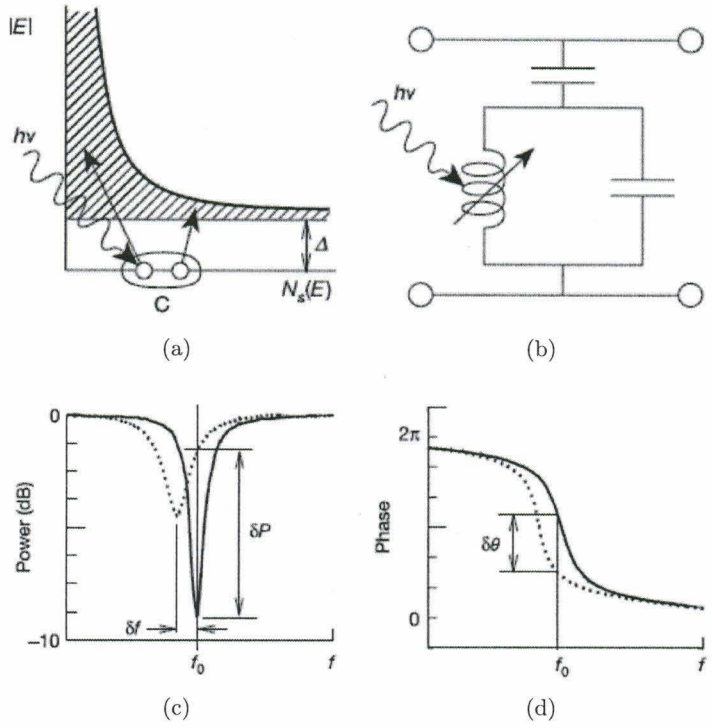

Figure 1.1: Schematic of the operation of KIDs. (a) shows an incoming photon with energy greater than the superconducting gap $h\nu > 2\Delta$ breaks Cooper pairs and excites electrons to the conduction band. (b) shows that the breaking pairs affects the inductance of our microresonators. (c) shows a change in depth and center frequency of our detector channel caused by pair breaking. (d) shows the shift in phase as the event occurs. This figure is reproduced from Day's *A broadband superconducting detector suitable for use in large arrays.* [3]

1.2.2 Frequency Multiplexing

Kinetic inductance detection is an attractive technology because it allows for natural frequency multiplexing. By tuning each detector to a different resonant frequency, multiple channels can be read out on the same line. If we have high quality factors, and therefore narrow linewidths, thousands of KIDs can be read out on a single transmission line. Natural frequency multiplexing allows KIDs to be scaled up to very large arrays and to meet next generation requirements on the focal plane.

In addition, we use large capacitors to bring down resonant frequencies to radio frequencies. This allows us to make use of room-temperature amplifiers and co-axial cables which both a simpler and cheaper solution compared to using SQUIDs to readout TES arrays.

1.3 Principle operation of SuperSpec

SuperSpec is an on-chip lithographed spectrometer that covers the submm/mm bands. The basic architecture is a filterbank consisting of superconducting microresonators. A full instrument would contain order 500-channels on a few square centimeters of silicon.

1.3.1 Circuit Model

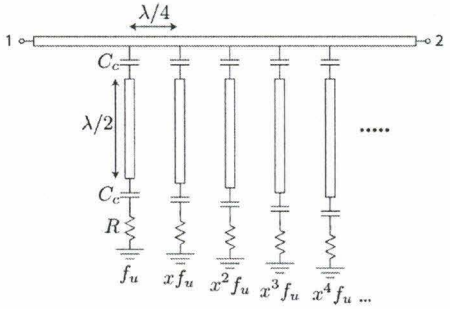

Figure 1.2: Transmission line concept of SuperSpec. Image reprinted from Kovac's Transmission-Line Resonator Spectrometers [9].

Radiation is captured by an antenna and propagates down a transmission line past N_c tuned resonant filters comprised of $\lambda/2$ transmission line resonators. Channels are spaced in frequency space by a geometric progression with ratio x. The resonant frequencies of the filters are $f, xf, x^2f, \cdots$, etc. These channels couple both to the feedline and to power detectors. These channels are spaced $\lambda_i/4$. In a filterbank with oversampled channels, this spacing minimizes interchannel crosstalk.

1.3.2 Lithographed features

SuperSpec design is implemented using superconducting microresonators [1], [16], [15]. The lithographed circuit is shown in figure 1.3. Filter resonators are $\lambda/2$ transmission line resonators that are bent into a "staple" configuration. These filters are inductively coupled to the main feedline and capacitively coupled to the detector.

Power is deposited on the detector, which is comprised of an inductive titanium nitride meander and an interdigitated capacitor. The breaking of Cooper pairs causes a shift in the detector's inductance which causes a resonant frequency shift $\omega = (LC)^{-\frac{1}{2}}$. Each KID is coupled to a coplanar waveguide readout feedline. By continuously measuring the amplitude and phase of a microwave tone coupled to the resonator, we can measure the frequency shift of the resonator and thus the power absorbed by each detector.

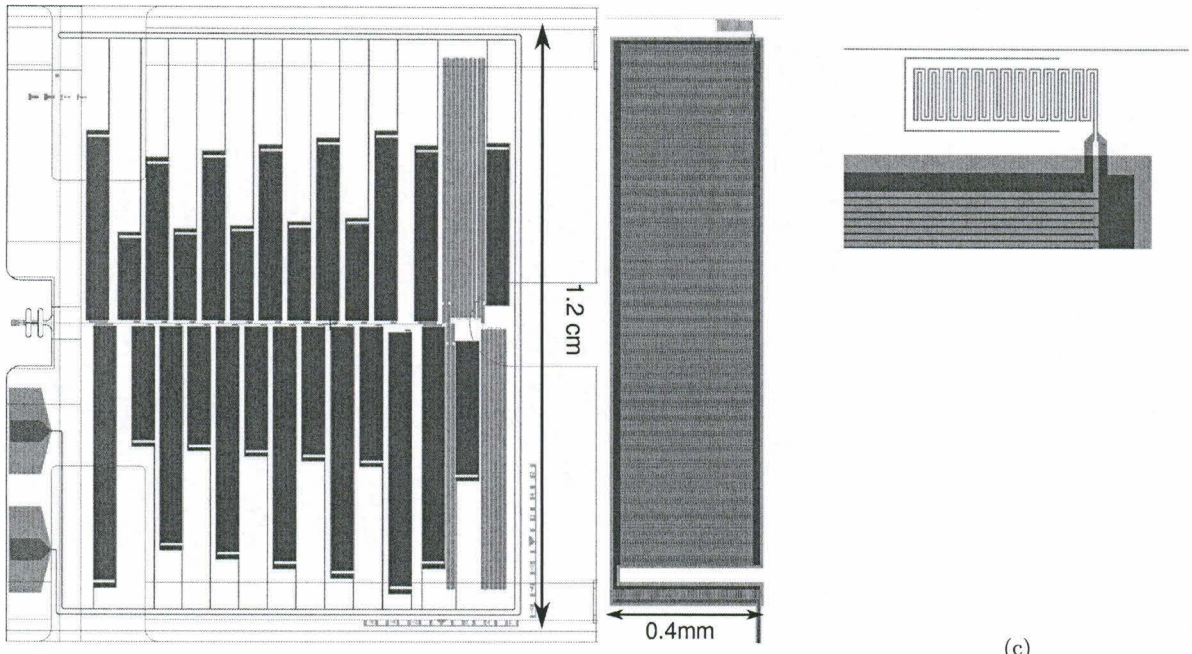

(a) (b) (c)

Figure 1.3: Prototype spectrometer chip layout. (a) shows a broad picture of the chip. Radiation is coupled into the system through the slot antennas and propagates down the main feedline. 24 channels are coupled to the feedline shown in gold. The structures on the right are dark channels and other test structures. (b) zooms into one channel. We see the mm-wave features in green coupled to a small inductor and a large interdigitated capacitor. The bottom shows co-planar waveguide structures for readout circuitry. (c) shows a further zoomed in image of the half-wave resonator and inductor. These images are re-printed from Shirokoff's ObsCos Seminar talk from 2014/04/03.

SuperSpec uses an inverted microstrip geometry as the mm-wave transmission line. Microstrip provides several advantages to alternative waveguide structures. The confinement of electric fields and continuous ground plane between channels in microstrip reduces radiative losses, interchannel cross talk, and coupling of KID resonators in their environment.

Niobium is the material of choice for the mm-wave features. It is superconductive and lossless at our two target bands at the $1300\mu m$ window (180-330GHz) and 850 and 650 μm window (350-550GHz). The kinetic inductance detector is made from TiN, which has several important properties. The composition of the TiN_x films allows for a tunable T_c up to 5K. Lower T_c superconductors create more sensitive detectors, at the expense of requiring colder cryogenics. TiN has high normal state impedance providing high detector response, and has an order of magnitude higher internal Qs ($Q_i \sim 10^7$) than other candidate materials such as aluminum [10].

1.4 KID Sensitivity

Sensitivity of our detector depends on the magnitude of response and on the noise present in the detector and readout electronics. A fundamental source of noise in our system is generation-recombination (GR) noise. Random fluctuations in quasiparticle density, caused by spontaneous breaking and recombining of Cooper pairs, ultimately set the sensitivity limit of our device [18]. There are two major terms in GR noise, one arising from thermal phonons and another from optical photons breaking pairs. By decreasing the temperature of operation, and keeping the superconducting gap energy Δ high, we can bring thermal GR noise to levels below background noise.

Two-level system (TLS) noise is believed to be caused by capacitive fluctuations in amorphous dielectric [4]. This source of noise is not fundamental limit because it does not occur in the kinetic inductance element. We can decrease TLS noise in principle by increasing the capacitive area of the IDC or by switching dielectrics to one with a more constrained lattice.

Noise-equivalent power (NEP) is the measure of sensitivity of a detector. NEP is defined as the incident power required to give a signal to noise ratio of unity over $0.5s$ of integration. In the case we have a TLS noise limited device, the NEP is dominated by TLS contribution to NEP,

$$NEP_{TLS} = \frac{\sqrt{S_{xx,TLS}}}{R}$$

where S_{xx} is the noise spectrum, $x \sim \frac{\delta f}{f} \sim \frac{\delta L}{L}$ is the fractional frequency shift and $R = \frac{\delta x}{\delta P}$ is the fractional frequency responsivity [7]. If power deposited is kept constant as we decrease inductor volume, than quasiparticle density n_{qp} increases resulting in increased sensitivity. Conversely if we can increase the power deposited without requiring more inductor volume, we also gain more sensitivity [18].

In this thesis we explored electromagnetic designs that would improve responsitivity and improve sensitivity. We took two approaches. We pursued higher quasiparticle density by decreasing inductor volume. We also explored increasing the efficiency of each detector through electromagnetic design. Additionally, we looked at how to build a full filterbank to obtain the highest signal to noise in each channel in order to best detect a line.

Chapter 2

Decreasing Detector Volume to Improve Sensitivity

Minimizing the detector volume can be a straightforward way to increase the responsitivity of our detectors and ultimately improve sensitivity. In this thesis, we explored several potential paths to decreasing inductor volume.

2.1 Coupling Power from the half-wave resonator to the detector

In order to design a smaller inductive element that still has adequate coupling to absorb power, we have to understand how the detector couples to our half-wave resonator. A general two-conductor system has both capacitive and inductive coupling. Capacitive coupling occurs when electric fields from one conductor leak to a neighboring conductor. Inductive coupling occurs when currents in one conductor produce magnetic fields that induce a voltage across another conductor through magnetic induction.

Half-wave transmission lines are compact way to produce a notch filter. In a open-circuited transmission line, the ends of the transmission line create boundary conditions where currents are zero, $J = 0$, which also produce regions of high electric fields. Conversely, the current in the center of the transmission line is maximized.

The geometry of a half-wave transmission line influences how power is coupled from the main feedline and from the half-wave transmission line to the detector. An efficient $\lambda/2$ transmission line is bent into a staple as shown in figure 2.1. The long legs of the staple couple inductively from the feedline into the transmission line resonator. The ends of the staple section alternate in high and low voltage. When the detector is placed between the two legs of the staple, the potential difference capacitively drives current in the lossy material.

We can confirm that this intuitive model matches simulation results. We can create an inductive meander oriented in two directions as shown in figure 2.1b and figure 2.1c. If the meander lines are parallel to the

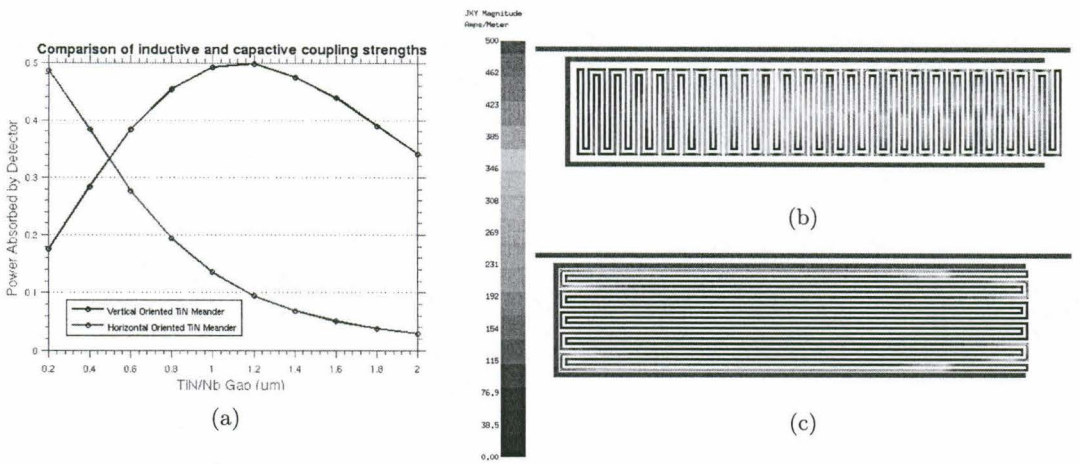

Figure 2.1: A simulation of time-averaged currents in TiN meander. The meander is the induction portion of the KID. The solid red line features are Nb microstrip with currents off scale. Input and output ports are located along the top feed. The two current plots compare of inductive (bottom) and capacitive (top) coupling. We see much higher volume of the TiN activated in a capacitive coupled detector.

legs, the detector is optimized for inductive coupling because the long traces faciliate driving of currents. If the meander lines are perpendicular to the legs of the line, then the potential difference in the staple should drive currents in our detector.

We varied the coupling distance between the TiN meanders, acting as a resistive detector, to the Nb staple for these two meandered geometries. This modulates the strength of coupling between the Nb staple and the resitive material, which ultimately affects what impedance the detector is in a circuit model. Figure 2.1a shows curves relating the TiN/Nb gap to the power absorbed. The curve for the vertically oriented meander, coupling primarily through capacitive coupling, shows that we have an optimal coupling distance of $\sim 1.1\mu m$ between the niobium and the TiN. The curve for the horizontally oriented meander requires a much closer coupling distance of $\sim .2\mu m$ between the niobium and TiN. Because of the much smaller gap required to get critical coupling, the inductor geometry poorly couples to our staple. These results show that an optimal geometry that couples most efficiently to our staple requires vertical traces of TiN in order to capacitively couple and dissipate power.

2.2 $\lambda/2$ Transmission Line Filter Geometry

A straight forward approach to minimizing inductor volume is to change the aspect ratio of the staple, which is defined as ratio between the legs of the staple and the center section. A constrained optimization will show that, for a given desired staple length, the maximum area in the staple occurs when the center section is twice as long as the legs. The minimum area is approached in the degenerate case when we take the center

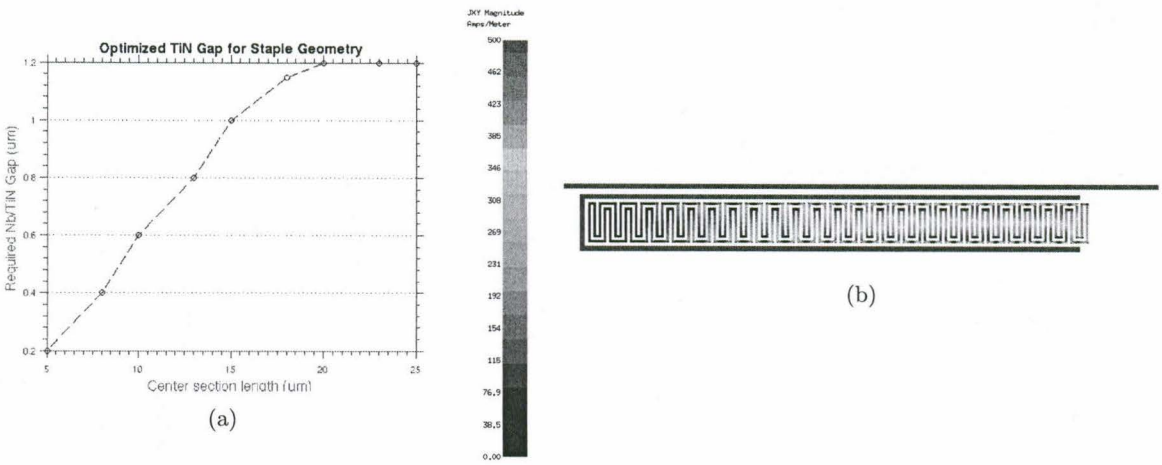

Figure 2.2: Required TiN/Nb coupling gap as we change the $\lambda/2$ transmission line geometry. Even for very elongated staples, we can get critical coupling within our machine tolerances.

section length to zero.

By decreasing the center section of the staple, we decrease the amount of resistive material required to fill the space in the staple. From an energetic standpoint, we need higher coupling. We need to dissipate the same amount of power in less resistance, which can be accomplished by increasing the current in our resistor. We are required to have a stronger coupled detector to drive higher currents. This is obtained through decreasing the TiN/Nb coupling distance.

Figure 2.2a shows that as we decrease the center staple length we have to decrease the TiN gap in conjunction. A conservative estimate for our fabrication tolerances is $0.5\mu m$ alignment of two different metals. Figure 2.2a tells us that we can decrease this center section from our current design value of $\sim 20\mu m$ to less than $10\mu m$ resulting in a factor of 2 decrease in inductor volume.

2.3 Removing Inductor material

Figure 2.1b and figure 2.2b show that large regions of our inductor is not active. No power is being dissipated in the inductor near the bend of the staple. We can cut out parts of the inductive portion to further drive up quasiparticle density n_{qp} and increase the response of our detector.

Figure 2.3a show comparisons between two different staple geometries. The red and blue curve shows staples with a center section of $10\mu m$ and $20\mu m$ respectively with the TiN/Nb gap that we optimized above as shown in figure 2.2a. Figure 2.3a shows that even removing 50% of the inductor volume results in high power deposition. The purple curve shows a $20\mu m$ staple where we pulled in the TiN/Nb gap to $0.6\mu m$ which is the gap required for a $10\mu m$ staple. We see that optimal coupling occurs when we have 75% of the

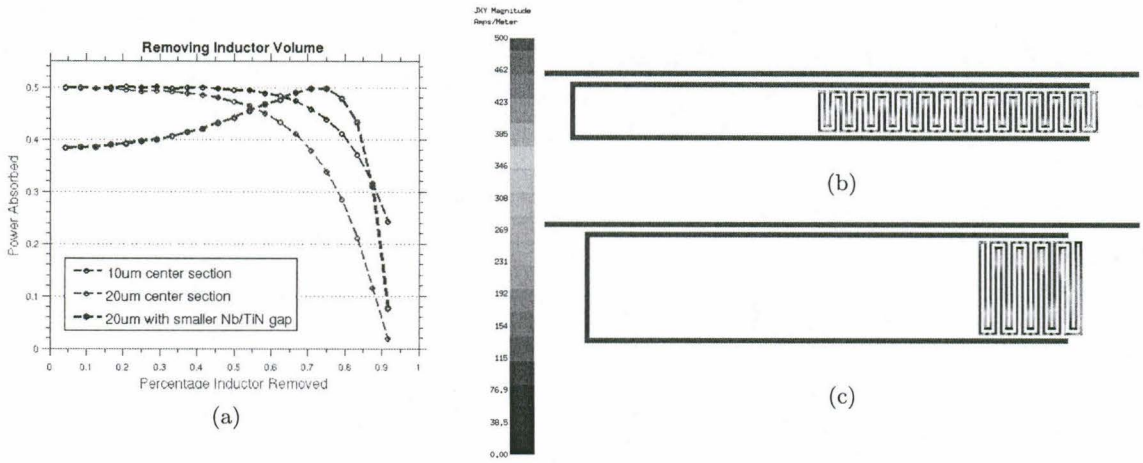

Figure 2.3: Analysis of low-inductor volume systems. We still get sufficient power coupling even as we remove half of the inductive material.

inductor removed.

Figure 2.3b and Figure 2.3c show the minimal inductor volume for their respective staple geometry. These simulation suggest that there is a minimum inductor volume for a given TiN/Nb gap requirement. The $10\mu m$ configuration has a volume a factor of four smaller than the standard $20\mu m$ staple because it has half the width and half the height. The $20\mu m$ with stronger coupling also has a factor of four smaller inductor volume. It has the same height, but only a quarter of the width of the standard channel when we pull the TiN gap closer in.

Ultimately the inductor volume is limited on our fabrication tolerances. Small gaps are sensitive to lithographic inaccuracies. We conservatively estimate that we can align metals within $0.1\mu m$ and space two different metals apart no closer than $0.5\mu m$ to be confident we have no electrical contact. This limits us to inductor volumes around $\sim \times 4$ smaller than our current design values for $R \sim 150$ channels.

2.4 Inductor Patterning

Changing the inductor patterning could possibly increase the effectiveness of coupling power from the inductor to our staple. We showed earlier that the dominant source of coupling is through capacitive coupling caused by ends of the staple setting a potential difference to drive current in our inductor. We suspected that geometries with maximal vertical sections would have stronger coupling.

We can measure how strongly a given geometry couples to the staple by finding the optimal TiN/Nb coupling gap in order to get 50% coupling into our detector. If a geometry requires smaller gaps, or stronger TiN/Nb coupling to get the same power across, then the geometry naturally is less well coupled to the staple.

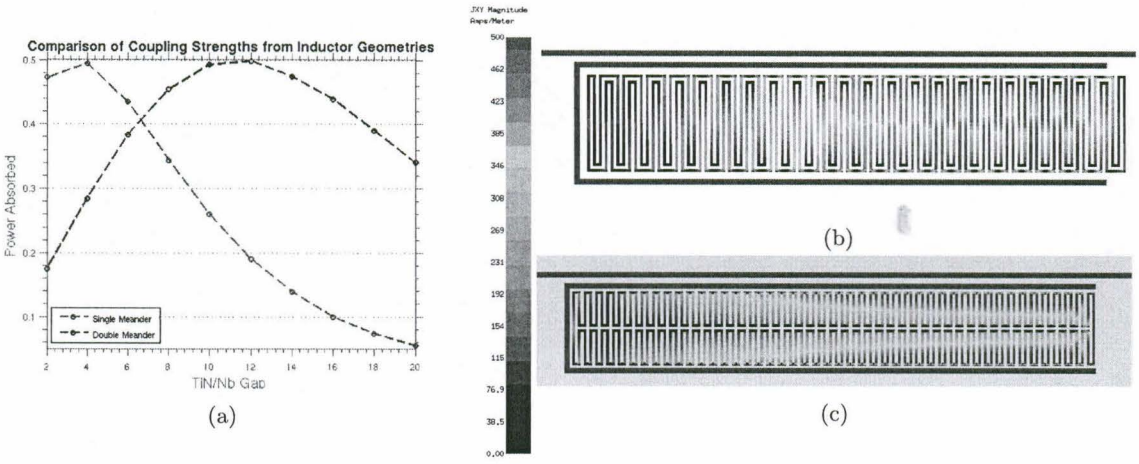

Figure 2.4: Comparison of the double meander (figure 2.4b) to the single meander (figure 2.4c).

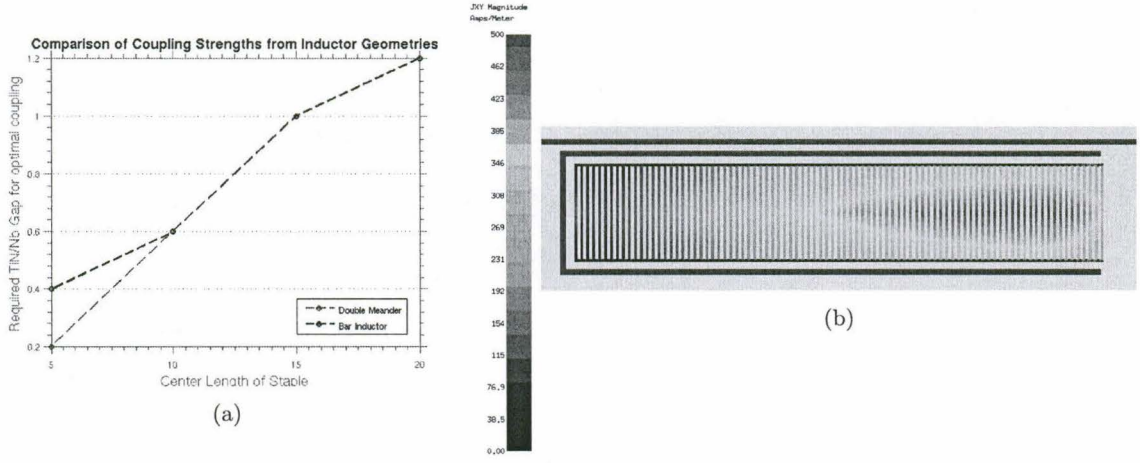

Figure 2.5: Comparison of the bar inductor to double-meander. Both these geometries maximize vertical section length for a given inductor shape.

Figure 2.4 compares two inductor patterns, a single meandered to a double meandered line. For a double meandered, the current is distributed towards the center of the inductor. The single meander introduces a boundary condition $J = 0$ at the center of the meander which significantly impacts how much power flows through the system. Figure 2.4a shows that the single meandered line geometry is worse at coupling and requires smaller gaps to obtain the same coupling.

Figure 2.5 compares two inductor patterns, a bar pattern and a double-meandered line. The bars geometry should provide the most efficient power coupling for a capacitively coupled detector. The long straight sections of TiN are maximized in this geometry. Figure 2.5b shows uniform currents throughout the inductor. Figure 2.5 shows that the required TiN gap for a given staple geometry is the same as the TiN gap for the double meandered line until we reach very small center sections. When the staple is highly elongated, the

bar inductor outperforms the double meandered and requires a $0.4\mu m$ coupling gap while the meandered line requires a much closer $0.2\mu m$ coupling gap.

While the bar pattern provides high coupling, it is non-ideal for single-detector applications. The inductance of the pattern is extremely low because the lines of the TiN are connected in parallel. We would need overwhelmingly large capacitors to bring readout frequencies to our desired values. In addition, the parasitic inductance of the interdigitated capacitor would become a large concern because the response of a detector is the fractional change in total inductance and the inductor must dominant the detector's inductance to get high responsitivity. The double backed meander remains to be the best inductor patterning to provide strong coupling.

2.5 Conclusion

There are several avenues for reducing inductor volume in order to improve responsitivity and NEP. With no perturbation to our current transmission line filter design, we can decrease inductor volume by a factor of two. With minor changes to the staple, by pulling the TiN/Nb coupling gap closer together, and elongating the staple, we can reliably get a factor of four.

When we decrease inductor volume, we increase the readout frequencies because the detector simply acts as an LC circuit $\omega^2 = (LC)^{-1}$. In principle we could increase our capacitor area to readjust our readout frequencies to our desired values. This would not only bring down the readout frequencies, which would be convenient with our system's readout electronics, but would also improve our sensitivities by reducing TLS noise.

However we are already have large capacitors relative to our inductors. Even a factor of two increase in capacitor area would be unwieldy when we are aiming for a ~ 500 channel filterbank.

Low inductor volume is ultimately limited by coupling between the TiN and the resonant staple. We physically cannot get more coupling because there is a limit to how close we can move our TiN to the niobium. Further decreases in volume would require revisiting the dielectric stack. We could, in principle, get higher coupling by removing notches in the ground plane. Microstrip fields would be less confined and couple better to the detector. However this would introduce complications. Removing the ground plane would cause impedance mismatches in the feedline, and lead to reflected power and resonances along the line. In addition we would introduce radiative losses in our system.

Another potential way of increasing coupling is placing the TiN in layers between the niobium feedline and the ground plane. Field lines from the niobium directly see the TiN. However this would require an additional lithography step and complicate the overall design.

Chapter 3

Electromagnetic Design of More Efficient Detectors

3.1 Half Wave Transmission line

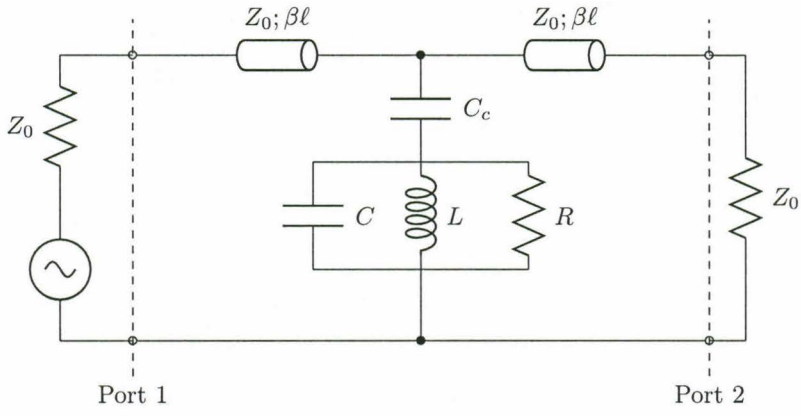

Figure 3.1: Transmission line model of a single detector. We have a capacitively coupled RLC tank circuit.

Half-wave transmission lines are compact way to produce a notch filter. In a open-circuited transmission line, the ends of the transmission line are antinodes where voltage peaks. We typically bend the transmission line to create a staple so that the legs of the transmission line alternate in high and low voltage. When we place our detector in between the two legs, the potential difference capacitively drives current in the lossy material.

For an isolated detector on a transmission line, the circuit model is shown in figure 3.1. The analysis below will be analysis on resonance so that the reactive part of the detector impedance is 0 and we purely see a resistive element. The impedance looking into a lossless transmission line with characteristic impedance

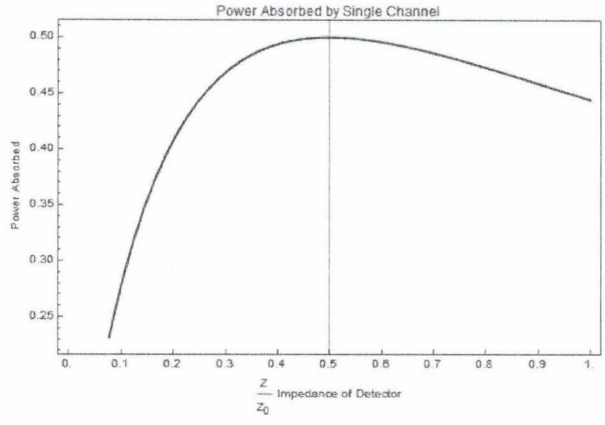

Figure 3.2: Power absorbed by detector as a function of detector impedance. We have max power absorption when the detector impedance is exactly one half the characteristic impedance of the feedline $Z = Z_0/2$.

Z_0 and length ℓ is,

$$Z_{in}(\beta\ell) = Z_0 \frac{Z_L + iZ_0 \tan(\beta\ell)}{Z_0 + iZ_L \tan(\beta\ell)} \tag{3.1}$$

where Z_L is the impedance of load on the end of the transmission line and β is the wavenumber at a certain frequency. We have matched ports so that the transmission line looking away from our detector is simply $Z_{in} = Z_0$ which is independent of frequency.

The load of the first transmission line is then the parallel impedance $Z_L' = \frac{Z_D Z_0}{Z_D + Z_0}$ where Z_D is the impedance of our detector. Because there is an impedance mismatch between the transmission line and the load, voltage would be reflected with amplitude,

$$\Gamma = \frac{Z_L' - Z_0}{Z_L' + Z_0} = -\frac{Z_0^2}{2Z_D Z_0 + Z_0^2} = -\frac{Z_0}{2Z_D + Z_0} \tag{3.2}$$

We want to find the power deposited on our detector. Power delivered for an AC circuit is $P = \frac{1}{2} IV^*$, which allows us to take the ratio between the power to the detector to total power dissipated in the system, $P/P_T = I/I_T$ which using current division between the detector and port 2,

$$P = P_T \frac{Z_0}{Z_0 + Z_D} = (1 - |\Gamma|^2) \frac{Z_0}{Z + Z_0} \tag{3.3}$$

To prove that $Z = Z_0/2$ produces the maximum power, w simply plot the function numerically as shown in figure 3.2. The plot shows that we obtain a maximum when $Z = \frac{1}{2} Z_0$, and that power coupled to a half-wave resonator could not get more than 50% of power into our detector.

In this chapter, we explore schemes for improving upon this 50% maximum efficiency for a single isolated loaded resonator.

3.2 Ring Resonators

3.2.1 Introduction and Operation

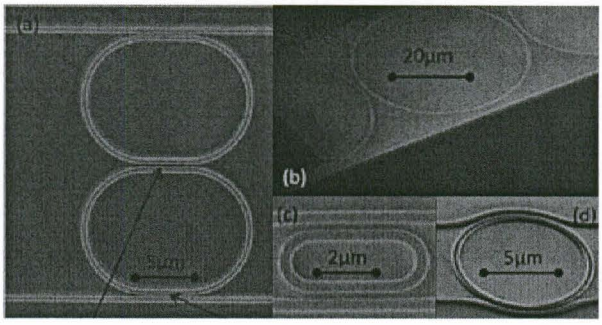

Figure 3.3: Figure showing silicon microring resonators in a variety of configurations and applications. Figure reprinted from Bogaert's review *Silicon microring resonators* in Laser Photonics Rev [2].

Ring resonators are used in silicon photonics in a variety of applications as spectral filters in the THz, optical switches for wavelength-division multiplexing, optical delay lines in photonic integrated circuts, sensing, and electro-optical modulators [2].

A generic ring resonator is composed of a self-looped waveguide. The principle behind operation is that the ring with perimeter length L supports resonances with wavelengths $L = n\lambda$. Traveling waves inside the ring constructively interfere with coupled waves from the main feedline. When coupled to two feedlines, the ring resonator pulls power from the main feedline to the second with unit efficiency

In the photonics community, ring resonators are typically made using dielectric waveguides and depend on using high index materials such as silicon. Modes are confined within the ring based on total-internal reflection. Waves grazing at a shallow angle will remain inside the dielectric.

3.2.2 Derivation of Unit Efficiency

The analysis of ring resonators in this section comes from Rabus's Integrated Ring Resonators [14]. We have two feedlines symmetrically coupled to a ring resonator. We define t_i is the self coupling coefficient of the electric field, κ_i is the coupling coefficient for an electric field from the ring to the feedline and α is the amplitude transmission of a wave that makes one pass through the ring and captures total waveguide loss. We assume lossless coupling so by power conservation, the power transmitted to self-coupling and cross-coupling waves sum to the incident power,

$$|t_i|^2 + |\kappa_i|^2 = 1 \tag{3.4}$$

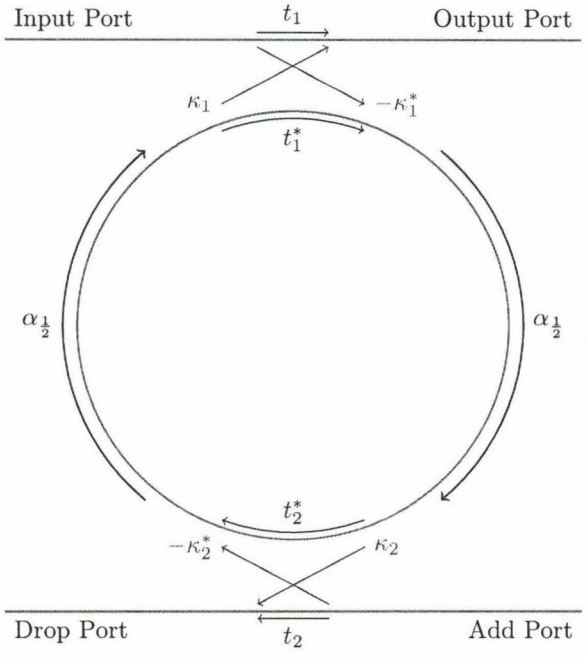

Figure 3.4: Model of a 4-port ring resonator. Self coupling coefficients are shown in blue, where cross coupling coefficients are shown in red. Loss around the ring is given in purple. Image replicated from Rabus, Integrated Ring Resonators [14].

For an incident electric field E_{i1}, we can find the electric field to the through port E_{t1} through by summing a geometric series. The fields transmitted is the sum of the fields that couple to the ring, pass through the loop an integer amount of time and couple back into the original waveguide.

$$\frac{E_{t1}}{E_{i1}} = t_1 - \kappa_1^*\kappa_1 t_2^*\alpha e^{i\theta} - \kappa_1^*\kappa_1(t_2^*)^2 t_1^*\alpha^2 e^{i\cdot 2\theta} - \kappa_1^*\kappa_1(t_2^*)^3(t_1^*)^2\alpha^3 e^{i\cdot 3\theta} + \cdots \tag{3.5}$$

$$= t_1 - |\kappa_1|^2 t_2^*\alpha e^{i\theta}\left[1 + t_1^* t_2^*\alpha e^{i\theta} + (t_1^* t_2^*)^2\alpha^2 e^{i\cdot 2\theta} + \cdots\right] \tag{3.6}$$

$$= t_1 - \frac{|\kappa_1|^2 t_2^*\alpha e^{i\theta}}{1 - t_1^* t_2^*\alpha e^{i\theta}} \tag{3.7}$$

$$= \frac{t_1 - |t_1|^2 t_2^*\alpha e^{i\theta} - |\kappa_1|^2 t_2^*\alpha e^{i\theta}}{1 - t_1^* t_2^*\alpha e^{i\theta}} \tag{3.8}$$

$$= \frac{t_1 - t_2^*\alpha e^{i\theta}}{1 - t_1^* t_2^*\alpha e^{i\theta}} \tag{3.9}$$

The field transmitted to the drop port can be found through a geometric series in a similar fashion where $\theta_{\frac{1}{2}}$ is the phase of a traveling wave accumulated traveling half the ring and $\alpha_{\frac{1}{2}}$ is the amplitude transmission of

a wave traveling half the ring.

$$\frac{E_{t2}}{E_{i1}} = -\kappa_1^*\kappa_2\alpha_{\frac{1}{2}}e^{i\theta\frac{1}{2}} - \kappa_1^* t_2^*\alpha t_1^*\kappa_2\alpha_{\frac{1}{2}}e^{i\theta+i\theta\frac{1}{2}} - \kappa_1^*(t_2^*\alpha t_1^*)^2\kappa_2\alpha_{\frac{1}{2}}e^{i\cdot 2\theta+i\theta\frac{1}{2}} + \cdots \tag{3.10}$$

$$= -\kappa_1^*\kappa_2\alpha_{\frac{1}{2}}e^{i\theta\frac{1}{2}}\left[1 + t_1^*t_2^*\alpha e^{i\theta} + \cdots\right] \tag{3.11}$$

$$= -\frac{\kappa_1^*\kappa_2\alpha_{\frac{1}{2}}e^{i\theta\frac{1}{2}}}{1 - t_1^*t_2^*\alpha e^{i\theta}} \tag{3.12}$$

If we are on resonance, then the length of the ring is a multiple of 2π so that $\theta = n\cdot 2\pi$ and our equations simply from $e^{i2\pi n} = 1$ and $e^{i\pi n} = -1$. We can then find the power by squaring the amplitude transmission,

$$P_{t1} = \left|\frac{E_{t1}}{E_{i1}}\right|^2_{\theta=2\pi n} = \frac{|t_1|^2 - (\alpha|t_2|)^2 - 2|t_1t_2|\alpha}{1 - 2|t_1t_2|\alpha + (\alpha|t_1t_2|)^2} \tag{3.13}$$

$$P_{t2} = \left|\frac{E_{t2}}{E_{i1}}\right|^2_{\theta=2\pi n} = \frac{|\kappa_1|^2|\kappa_2|^2\alpha}{1 - 2|t_1||t_2|\alpha + (\alpha|t_1t_2|)^2} = \frac{(1-|t_1|^2)(1-|t_2|)^2\alpha}{(1-\alpha|t_1t_2|)^2} \tag{3.14}$$

Notice that if we have a lossless ring $\alpha = 1$ and have symmetric coupling so that $t_1 = t_2$, equation 3.14 reduces to,

$$P_{t2} = \frac{(1-t^2)^2}{(1-t^2)^2} = 1 \tag{3.15}$$

If we have a lossy ring then optimal power transfer occurs when the coupling $\alpha t_2 = t_1$. This analysis tells us that ring resonators, on resonance, is capable of delivering 100% of power from the input port into the drop port, with no power passed down the feedline to the output port or the fourth port.

3.2.3 Ring Resonators in Microstrip

Microstrip differs from dielectric waveguides in several key ways. Microstrip lines are much more confined than dielectric waveguides. The strong confinement and large ground plane is naturally resistant to radiative losses and allows us to use a rectangular "ring" when constructing ring resonators from microstrip lines. However, strong confinement hinders coupling and in practice requires a long coupling section at least a wavelength long to reach unit efficiency.

Fundamentally the waveguide modes in microstrip is not-TEM, but quasi-TEM. In the limit we have very narrow spacing, the waveguide mode approach those of TEM. In our system, we have $0.5\mu m$ gap between the ground plane and microstrip line while the linewidths are $1um$ wide. Physically the even and odd modes of the coupled microstrip have different field distributions resulting in differing phase velocities [13]. The quasi-TEM nature of microstrip creates poor directivity in our ring resonator. Simulations show that our mm-wave geometry departs enough from a pure TEM analysis to prevent isolation in the fourth port in a

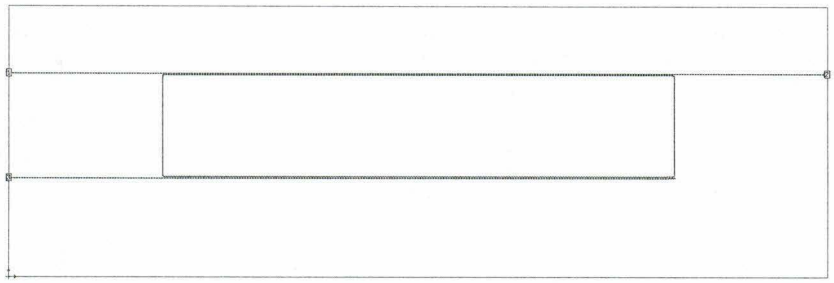

(a)

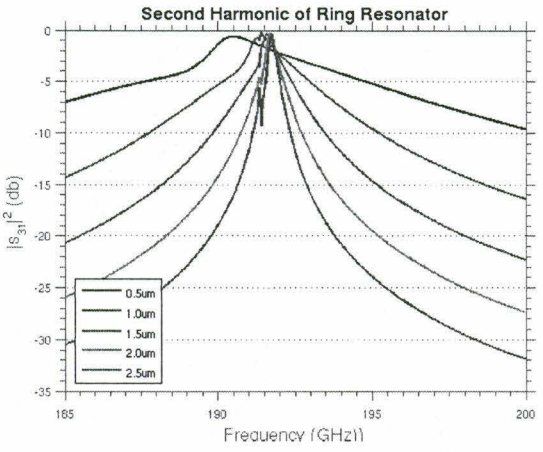

(b)

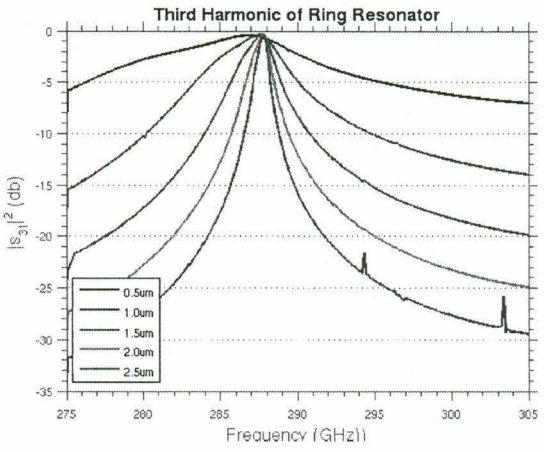

(c)

Figure 3.5: Simulation of a ring resonator showing transmission to the third port. The ring is shown in figure (a) and has total length $2mm$, linewith $1\mu m$ and a coupling length section of $850\mu m$. We vary the gap parameter. We see both the 2nd (c) and 3rd (d) harmonic peaks in our 180-330GHz band.

coupled line.

Figure 3.5 shows simulations of a 3-port ring-resonator with unit transmission. We varied the gap between the ring resonator and the feedline from $0.5\mu m$ to $2\mu m$ which results in $Q's \sim 20 - 800$ and preserves unit transmission to the drop port. These simulations show that ring resonators work in principle even using microstrip.

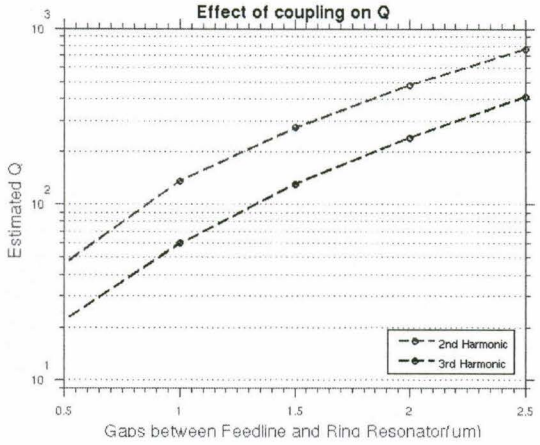

Figure 3.6: Estimated Q from the second and third harmonic peaks shown in figure 3.5

3.2.4 Conclusion

While higher efficiency is possible with ring resonators, we found that in practice this comes with drawbacks. In order to obtain adequate inductive coupling to set up traveling waves in the ring, we need a very long coupling section on the order of a wavelength long. This is prohibitive in a filterbank applications for several reasons. High order rings would have several harmonics in our band of interest. We would have to further filter out harmonics resulting in unnecessary complexity of the EM design. Additionally the long coupling section length results in a minimum factor of 4 $\times$ more real estate for each filter. This is prohibitive for a compact filterbank.

However this approach may be useful in bolometer type applications which would take advantage of the high efficiency, low Q filters. We are able to get $Q_s \sim 50$ for gap sizes of $1\mu m$. Higher harmonics would have even more wavelengths along the coupling section resulting in ultra low Qs without requiring exotic coupling schemes.

3.3 Backshorted Detectors

Backshorts are commonly used in bolometer type operations and are an effective wave to raise peak-power absorption. The system relies on destructive interference of the reflected wave. The principle is identical to a dielectric mirror. Light incident on a focal plane will reflect off due to the impedance mismatch between air and the detector. When the focal plane is suspended $\lambda/4$ above the ground plane, a wave will penetrate through, reflect off the backshort, and meet back at the surface of the detector after accumulating a 180° phase shift. The reflected wave destructively interfere, and the net effect is no reflection on resonance.

3.3.1 Derivation of unit efficiency

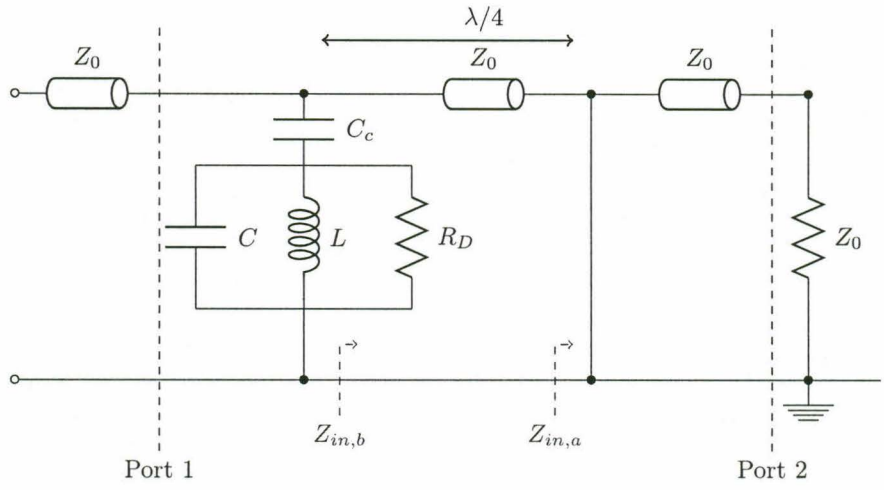

Figure 3.7: Transmission line model of a single backshort detector with impedance Z_D. Power propagates down port one to port two which is terminated with a matched load. The electrical short is placed a quarter-wavelength from the detector in order to set up destructive interference of the reflected wave. The blue lines $Z_{in,i}$ is the impedance looking into the circuit at those points.

In a filterbank, we cannot simply place a short in our transmission line because we have many channels, all operating at different frequencies, and a short would block power from traveling down the line. Instead we want a resonant reflect which can be made from an identical $\lambda/2$ transmission line resonator. For a general resonant detector, the scattering parameters are found [12],

$$s_{21}(x) = 1 - \frac{Q_r}{Q_c}\frac{1}{1 - 2iQ_r x} \tag{3.16}$$

$$s_{11}(x) = s_{21}(x) - 1 = -\frac{Q_r}{Q_c}\frac{1}{1 - 2iQ_r x} \tag{3.17}$$

where Q_r is the resonator Q, Q_c is the Q of an unloaded staple and x is the fractional frequency shift $x = \frac{f - f_0}{f_0}$. When we have no load impedance, then $Q_r = Q_c$. On resonance $x = 0$ and we have perfect reflection $s_{11}(0) = 1$ or otherwise we have an effective backshort on resonance.

We then want to show that in a transmission line model, we can obtain unity transmission to a backshorted detector. The circuit model for a detector + backshort pair is shown in figure 3.7 where we model the detector with impedance Z_L and the resonant reflector as having zero impedance or the short.In general if we have a transmission line length to be a quarter wavelength $\beta\ell = \pi/2$, from equation 3.1, we obtain a simple relationship between the load resistance on a quarter-wave transmission line and the impedance looking in,

$$Z_{in,\lambda/4} = \frac{Z_0^2}{Z_L} \tag{3.18}$$

The impedance looking into the backshort is zero because the parallel impedance of the backshort, and the load looking down the transmission line to port two is still zero, so according to figure 3.7, $Z_{in,a} = 0$. From equation 3.18 the impedance looking into the $\lambda/4$ section is infinite because $Z_L = Z_{in,a} = 0$ so that $Z_{in,b} = \infty$. The circuit simply reduces down to a loaded transmission line. The normalized power delievered to the detector is simply,

$$P = 1 - |\Gamma|^2 = 1 - \left|\frac{Z_D - Z_0}{Z_D + Z_0}\right|^2 \tag{3.19}$$

From inspection we can can easily see that if $Z_D = Z_0$ we have a matched load which results in no reflection of power and 100% power dissipation into the resistor.

3.3.2 Detector Impedance in a lithographed circuit

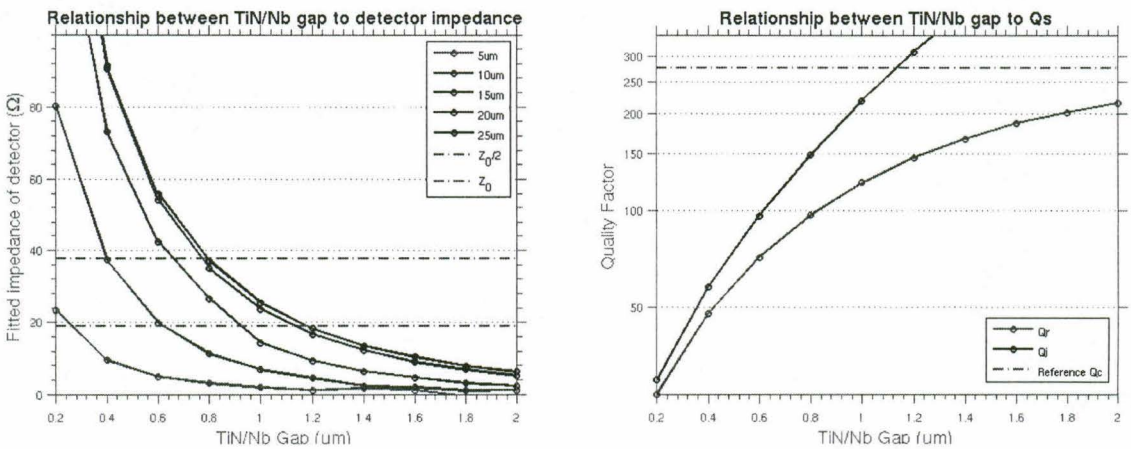

(a) (b)

Figure 3.8: TiN Gap and its scalings to physical parameters of impedance (a) and to Qs (b). In figure (a) we varied the staple's center section from $5\mu m$ to $25\mu m$. In figure (b) we kept the staple geometry constant with the center section at $20\mu m$.

It is clear from equation 3.19 that the impedance matching condition for a backshorted detector occurs when $Z_D = Z_0$. We want to find a relationship between physical geometric parameters in our lithographed circuit, to circuit impedance. Physically we can modulate the impedance of the detector by changing the gap spacing. The Nb/TiN gap spacing sets the coupling strength between the detector and our resonator. If we measure Q_r of the circuit, we can use the expression in equation 3.20 to find the equivalent impedance. The derivation of this expression is found in Appendix A.

$$Z_D(\omega_0) = \frac{Z_0}{2}\left(\frac{Q_c}{Q_r} - 1\right) \tag{3.20}$$

Figure 3.8a and figure 3.8b shows the dependance of TiN gap to design parameters impedance and Qs respectively. The lower dashed line corresponds to impedance $Z_0/2$ while the upper dashed line corresponds to impedance Z_0. These are the matching conditions for a single resonator detector and for a backshorted detector respectively. This graph tells us that we need a different Nb/TiN gap in order to get a well matched detector for the two different geometries. This is also reflected in equation 3.20. If we want a detector with impedance $Z_D = Z_0$ on resonance, we need to design the detector $Q_c = 3Qr$. This backshorted detector matching condition is different than a single detector, where we need to design $Q_c = Q_i = 2Q_r$ to get a well matched detector.

Figure 3.8a shows that impedance is dependent on the staple geometry. Physically this occurs because as we change the staple geometry we squeeze the amount of resistive material between the two staples. We need higher currents to go through less resistive material to keep power deposition the same. We obtain higher currents through stronger coupling.

3.3.3 Simulated Performance

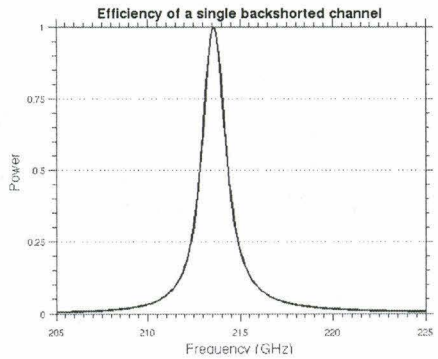

(a)

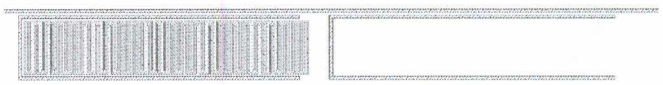

(b)

Figure 3.9: (a) Simulation of a single backshorted channel, showing power deposited $1 - |s_{11}|^2 - |s_{21}|^2$. (b) Sonnet geometry of the backshorted channel. Niobium traces are shown in red, while the TiN meander is shown in green. Port 1 and 2 are electrically attached to the feedline above (not shown). The reflector is spaced end to end from the detector by $\lambda/4$.

Using this predicted gap we can find the isolated performance of a backshorted channel. Figure 3.9a shows the performance of a well matched channel. We get unit efficiency on resonance with minimal out of band response.

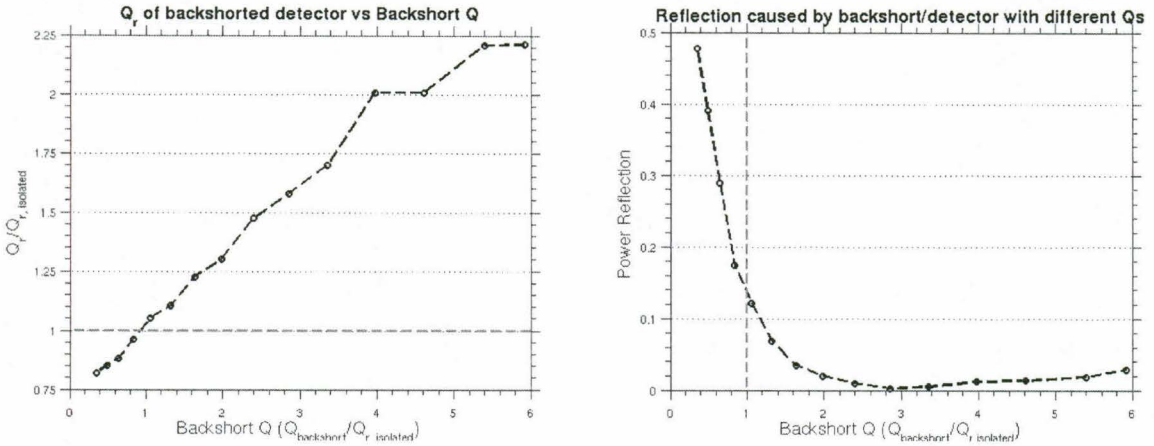

(a) (b)

Figure 3.10: Backshort Q and its effects on channel Q_r and reflection for the backshorted detector.

3.3.4 Backshort Q

The Q of the backshort becomes a design parameter in the backshorted detector scheme. We can increase the Q of the backshort reflector by changing the Nb/Nb spacing between the reflector staple and the main feedline. In conjunction, we must decrease the length of the reflector. This is because as we bring the reflector closer to the feedline, there is more coupling capacitance between the feedline and staple, which causes an additional shift in resonant frequency.

Figure 3.10a shows the dependence of the detector Q with the backshort Q. $Q_{r,\text{isolated}}$ is the channel Q when the backshort is removed. The intersection of the reference gray line, and the blue curve, show that when the reflector $Q_{\text{backshort}}$ matches the isolated detector $Q_{r,\text{isolated}}$, then the total Q_r remains the same.

Figure 3.10b shows out of band reflection caused by the backshorted detector. Plotted is the max reflection seen by port one as a function of normalized $Q_{\text{backshort}}$. We see that as we decrease $Q_{\text{backshort}}$, we get high out of band reflection. This behavior is expected because the backshort would be reflecting a lorentzian profile larger than what the detector could absorb. However it is unexpected that when the backshort $Q_{\text{backshort}} = Q_r$ is that we have high reflection $\sim$ 12% right off-resonance. We also have high reflection when the backshort Q_r is high. Physically the resonant reflector is not reflecting a large enough profile to set up destructive interference over the entire band. We end up with reflection from the detector. What is surprising is the minimum in figure 3.10b. The minimum does not occur when the backshort Q is matched with the resonator Q_r. Instead we get zero reflection when $Q_{\text{backshort}} = Q_c = 3Q_r$,

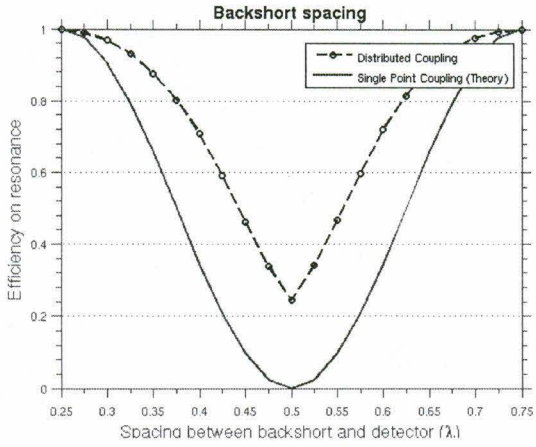

Figure 3.11: Performance of our backshorted detector as we adjust the spacing between the two resonators.

3.3.5 Backshort Spacing

The physics behind how the backshort work relies critically on the spacing between the backshort and our detector in order to set up destructive interference. Consider an analogous resonant system, a $\lambda/4$ dielectric mirror. We have a single point of reflection at the dielectric interface. Power transmission across this mirror follows $\sin(\theta)^2$ where $\theta = \beta\ell$ is the proxy for length [6].

We want to explore how close our system approximates this model with single, well defined point for reflection. Figure 3.11 shows the simulation of separating the resonator and its corresponding backshort. We see that despite the physics relying on resonant effects, we have very soft dependence in regard to spacing of the reflector. In addition we have large deviation from the single point coupled model. Even when the backshort is spaced $\lambda/2$ apart, when all power should be reflected and none transmitted, power still reaches the detector. This skewed function can be explained by distributed coupling, rather than point coupling, between the transmission line and staple. In the lithographed circuit, there is no single point of contact where we place the capacitive coupling between the feedline and the tank circuit. The resonant condition is smeared out. The distance from the detector to its reflector just has to be close to $\lambda/4$ which results in a system not terribly sensitive to errors in placing the backshort.

3.3.6 Backshort center frequency

The backshort relies on being a resonant reflector. We want to understand the system's response when the backshort is detuned caused by fabrication errors. We can modulate the transmission line length of the backshort, and hence its resonant frequency, and observe how frequency detuning degrades the performance of the system.

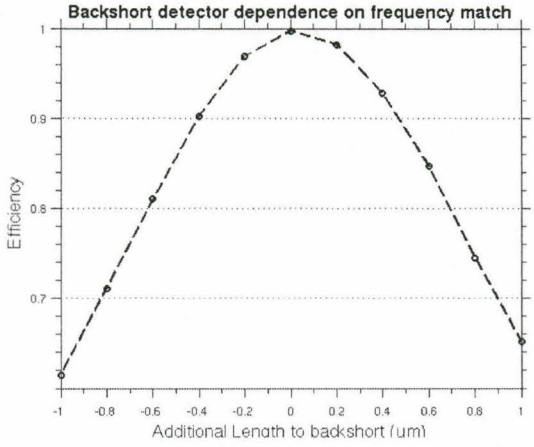

Figure 3.12: Tolerance studies on the backshort center frequency. We vary the backshort length from $\pm 1\mu m$ about the matched length, corresponding to a frequency shift of $\pm 1.04GHz$ about the center frequency.

Figure 3.12 shows how the efficiency of the system changes as we change the length of the backshort from $-1\mu m$ to $1\mu m$. For $1\mu m$ changes in lengths of our transmission line, we have a corresponding frequency shift of $\pm 1.04GHz$ from its center frequency. Our deposition process is reliable to about $\pm 0.1\mu m$ which results in corresponding shifts of $\pm 0.1GHz$. Figure 3.12 show that errors in our fabrication will cause $\sim 2\%$ decrease in efficiency so our fabrication tolerances will have no trouble creating effective backshorts.

3.3.7 TiN Gap Sensitivity

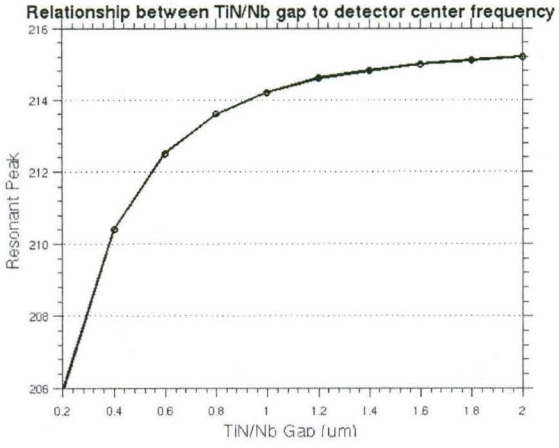

Figure 3.13: Dependence of resonator center frequency and TiN/Nb gap.

Changing the TiN gap causes two changes in our system. We have a different impedance to our detector, as shown previously in figure 3.8a. While this reduces peak efficiency of the backshort, the efficiency rolloff is soft with impedance. This is because power reflection is $\Gamma^2 = [(Z_L - Z_0)/(Z_L + Z_0)]^2$ which is a soft

function for $Z_L \sim Z_0$. The larger effect of modulating the TiN/Nb gap is changing the resonant frequency of the staple. A RLC resonance depends on the inductance, capacitance and impedance. Additional damping causes a decrease in the resonant frequency. In addition the presence of TiN changes the field lines of the microstrip. This propagates as changes to the inductance and capacitance of the transmission line resonator, leading to a shift in the resonant frequency.

Figure 3.13 shows how TiN influences the center frequency of a single channel without a backshort. As the TiN gets close to niobium, the gradient of $\delta f/\delta$gap becomes steeper. For $Z_D = Z_0$, we require the TiN/Nb gap to be $0.8\mu m$. Our fabrication tolerances can get the TiN/Nb gap to $\pm 0.05\mu m$ precision which results in a scatter in the resonant frequency of $\sim 1GHz$. Section 3.3.6 explored the relationship between frequency detuning and performance. The graph shows that a $\delta f \sim 0.5GHz$ between the resonator channel and the backshort would result in efficiency of 80% which is a dramatic reduction in performance. $\delta f \sim 1GHz$ results in efficiencies of 60% which destroys the performance of our backshort.

It would be difficult to create these backshort channels with current geometries due to tight TiN tolerances. However figure 3.13 shows that for large TiN/Nb gap, the gradient is much more shallow. This creates an opportunity for improvement. If we design a staple geometry and inductor pattern which require TiN/Nb gaps of $\sim 1.5\mu m$ then the tolerances on TiN would be acceptable. We would need geometries that naturally couple stronger, which returns to the problem explored earlier in chapter 2 of this thesis.

3.3.8 Conclusion

		Parameters		
Description	Change	Δf_0(GHz)	ΔQ	η
Feed to Resonator	$0.1\mu m$	0	10.2	98%
Feed to Reflector	$0.1\mu m$	0.1	10.2	99%
Nb/TiN Gap size	$0.1\mu m$	0	19	90%
Nb/TiN Gap offset	$0.1\mu m$	0	0	99%
Reflector Spacing	$0.1\mu m$	0	0	99%
Reflector Linewidth	$0.1\mu m$	0.6	78.9	56%
Resonator Line Width	$0.1\mu m$	1.1	81.4	53%
TiN Line Width	$0.05\mu m$	0	0	99%
Resitivity	20%	0	10.1	99%
SiN Thickness	10%	-1.1	33.3	96%
SiN permitivitity ϵ_r	10%	6.2	-20.3	96%

Table 3.1: Tolerances for backshorted detector. We took estimates of our lithography capabilities and observed how errors in lithography would propagate into the performance of the detector.

Resonant reflectors are an effective and compact way to deliver 100% power to our detectors. However

the effect critically depends on getting both the detector resonator and the backshort resonator to match frequencies. A small change in TiN gap spacing of $0.1\mu m$ would cause a decrease in performance of 10%. If the backshort detector linewidth was different from the resonator detector linewidth by $0.1\mu m$ then there would be a frequency mismatch $\Delta f_0 \sim 1GHz$ which would also destroy the effect. Backshorted detectors work in principle of delivering higher power, but the geometry is much more sensitive to errors in lithography.

Chapter 4

Filterbank Design

The Kovacs and Zmuidzinas memo gives a general design procedure for a general transmission-line resonator spcectrometer [9]. We repeat the equations here for completeness. A spectrometer with desired bandwidth $f_l \leq f \leq f_u$ with resolution $\mathcal{R} = f/\Delta f$ and spcetral channel number N_c can be built by spacing the channels in geometric progression $f_u, xf_u, x^2 f_u, \cdots x^{N_c-1} f_u$. The frequency scaling factor is given by,

$$x = \exp\left(-\frac{\ln f_u - \ln f_l}{N_c - 1}\right) \tag{4.1}$$

The number of channels is chosen with dependence on both the spectral resolution, and a over-sampling factor of Σ.

$$N_c = \Sigma \mathcal{R} \ln(f_u/f_l) \tag{4.2}$$

High over-sampling factors give higher peak absorption over the whole band, at the expense of requiring more detectors and each individual detector sees less power.

4.1 Channel design considerations

The ideal filterbank would be composed of perfectly square notch filters with unit absorption on resonance and no absorption or reflection out of band. We would have no cross-talk between channels with different center frequencies, and the tunability of width allows us to target any Qs.

It is difficult to design the ideal channel that can generalize to a full filterbank. Channels on filterbanks inherently interact with one another. Channels in front will absorb power at higher frequencies. Channels behind will reflect back power at lower frequencies.

Because channels in a full filterbank do not see the full, uninterrupted power profile, they fundamentally behave differently from single channel simulations. It is not sufficient to design the ideal channel without

placing it in a filterbank to see how it behaves.

We can study the interaction of channels by simulating partial filterbanks and observing the response of each detector at all frequencies. The middle channels in a partial filterbank are representative of how a channel in a total filterbank would behave. We outline two different methods to approaching this problem in Appendix D and Appendix E. The plots below have been generated through numerical analysis of filterbanks.

There are two approaches we explored to creating a better channel. One is stringing together multiple log-space resonators to make a single channel. In the limit we have infnitely high Q detetctors and high oversampling factors, we get a square band pass. Alternatively we can use the backshorted detectors we have analyzed in chapter 3 to create filterbanks.

4.2 Signal to Noise Ratio

The signal to noise is the metric to measure channel performance. The signal is the normalized, average power between the full width half max of a single channel. If we assume we are in the photon noise limit, then the noise scales as the square root of the total integrated profile. We normalize with the full width half max. If $\Delta\nu$ is the FWHM, then the normalized signal to noise is,

$$\text{SNR} = \frac{\frac{1}{\Delta\nu}\int_{-\Delta\nu/2}^{\Delta\nu/2} P(\omega)\, d\omega}{\sqrt{\frac{1}{\Delta\nu}\int_{-\infty}^{\infty} P(\omega) d\omega}} \tag{4.3}$$

4.2.1 Paired log-spaced Detectors

Log-spaced detectors read out in chunks can have high signal to noise. The more channels read out together, the more square the bandpass becomes and our SNR ratios improves. Figure 4.1 shows simulations of channels with varying number of log-spaced detectors at a number of different oversampling factor Σ. We keep channel R constant throughout this simulation. Each individual detector had increased Q with $Q_r = R * n$ where n was the number of detectors..

Figure 4.1a show that increasing the number of detectors in a channel increases signal to noise. However the approach to unity is slow, because of the large wings of Lorentzian profiles. In addition, oversampling log-spaced detectors directly improves peak power absorbed. The gains in SNR plateu as $\Sigma \sim 1.5$.

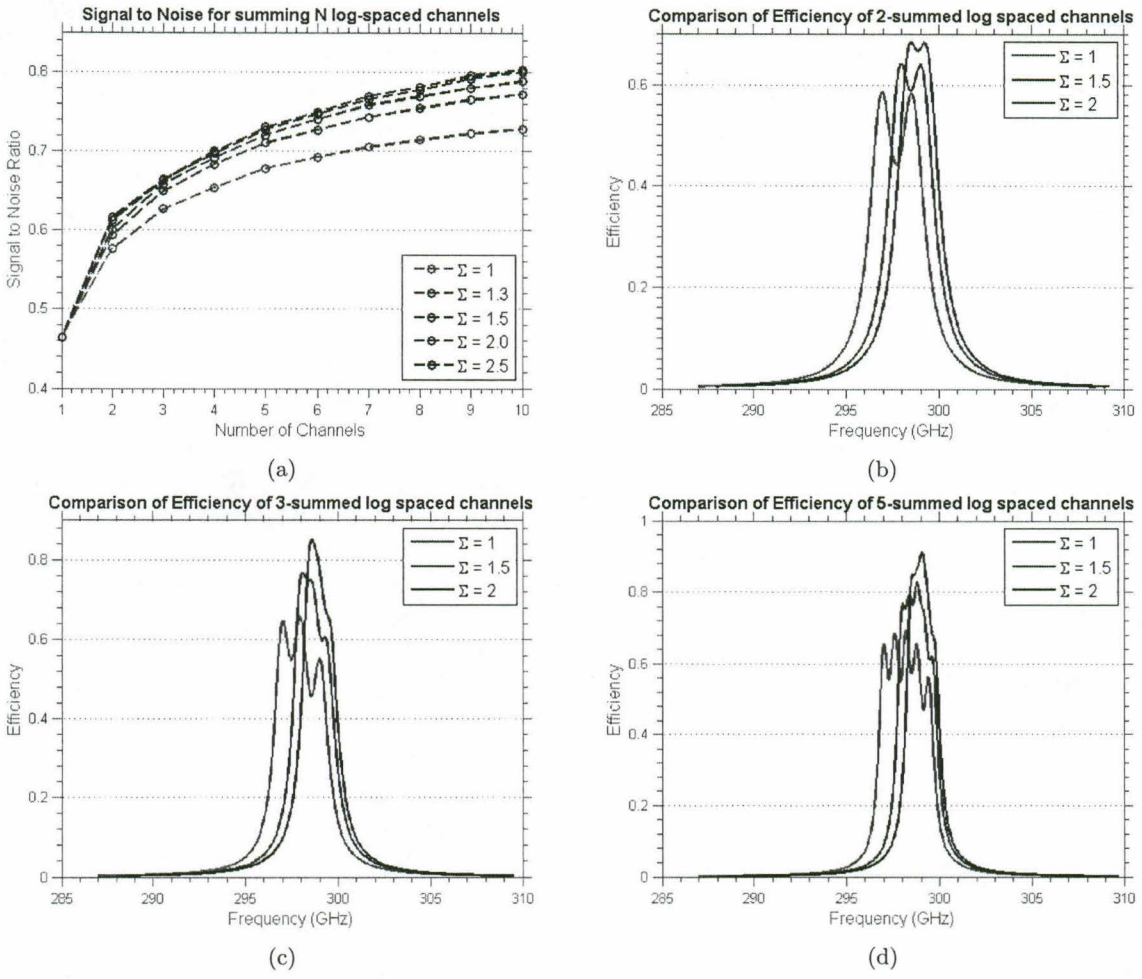

Figure 4.1: (a) shows the signal to noise ratio for n-number of detectors read out together at various oversampling ratios. (b,c,d) Profiles of n-log spaced channels read out in chunks with differing oversampling ratios.

4.2.2 Backshorted Detectors in filterbanks

Backshorts are a reliable way to increase efficiency in our system. In chapter 3.3 we showed that we can get 100% power to the detectors.

We want to find a backshorted detector that is most efficient in a filterbank. We can explore the backshort parameter space in order to find one with the highest signal-to-noise ratio. There are two main parameters which can cause broadening of our features and reduction of wings.

The first is the backshort Q. If we increase the Q of the backshort so that $Q_{\text{backshort}} = Q_c$, then we would have zero reflection, at the cost of having larger wings. However when the Q of the resonator-detector and backshort is matched, we have a more square profile with reflection of about 12%. The ideal $Q_{\text{backshort}}$ is somewhere between the two. The second parameter is the impedance of the detector. While $Z_D = Z_0$ is

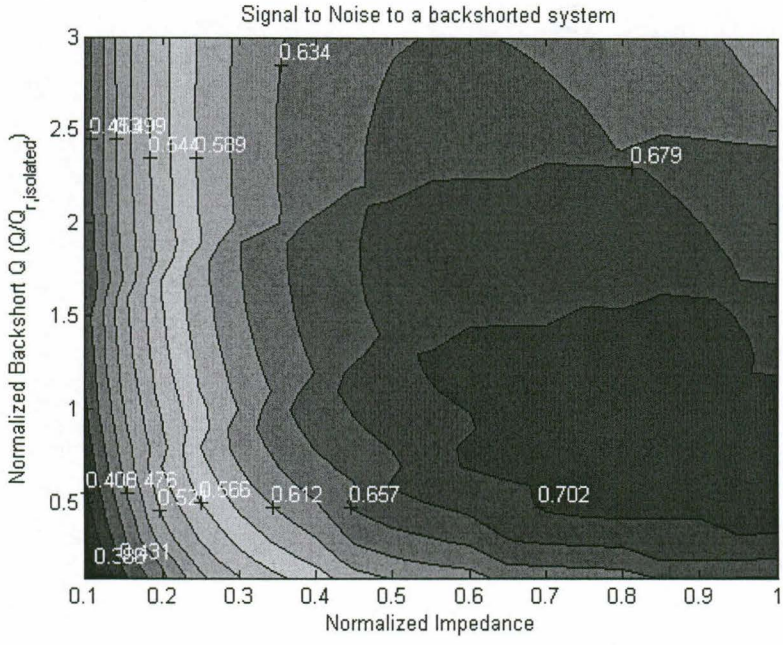

Figure 4.2: Contour plot of backshorted detector. By varying the two free parameters, $Q_{\text{backshort}}$ and Z_D, we can get a factor of 2 change in signal to noise of the channel.

the condition for peak efficiency, it produces narrow linewidths. Decreasing the impedance would broaden the peak and increase the signal.

Figure 4.2 shows how signal to noise behaves under the two parameters we described. The maximum signal to noise in this graph is 0.725 and occurs when the detector impedance is $Z_D = Z_0$ and the backshort is at very low $Q = Q_{r,\text{isolated}} * 0.4$. This arrangement would make a poor channel for a filterbank due to high reflection. Figure 3.10b shows that we would have 30% reflection which would be prohibitive for our applications.

Figure 4.3 shows the family of curves of signal to noise vs backshort Qs. We see that the signal to noise function has fairly soft dependence on both Qs and impedance while the reflection curve is much steeper to both parameters. An optimal channel would have acceptable reflection for our backshorted detector but maintain very high SNR.

If we allow 5% reflection caused by the backshort, then the highest SNR ratio we can obtain is ~ 0.71 when $Z_D = 0.8Z_0$ and $Q_{\text{backshort}} = 1.6 * Q_{r,\text{isolated}}$. This is fairly close to the maximum signal to noise with dramatically less reflection.

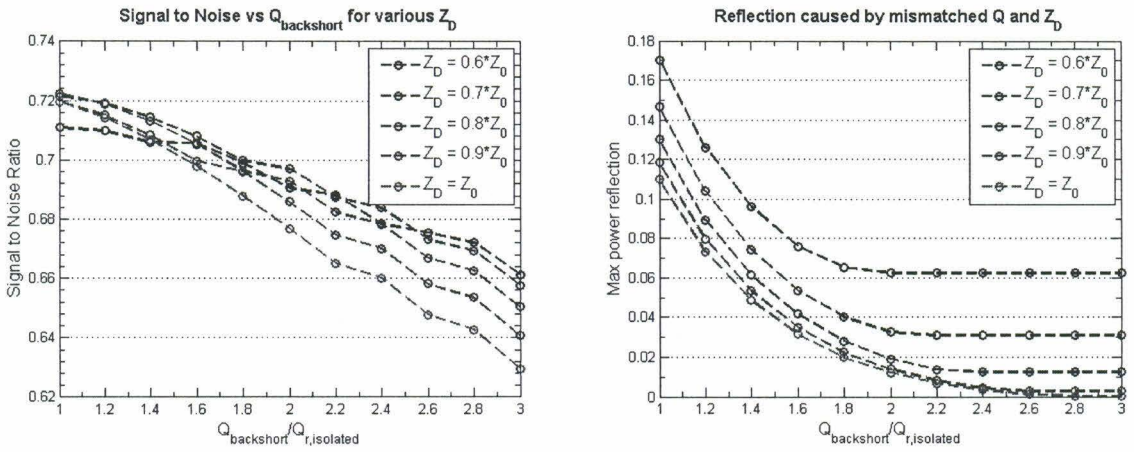

(a) (b)

Figure 4.3: Signal to Noise and reflection curves as we vary both $Q_{\text{backshort}}$ and Z_D

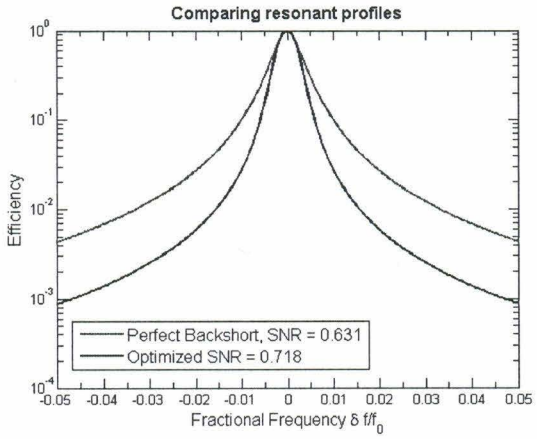

Figure 4.4: Comparison between a perfect backshort detector to an optimized SNR.

4.3 Filterbank Simulations

Ultimately we want to use these channels to create full filterbanks. We numerically simulated filterbanks using four different architectures. The first is simply a 10 channel filterbank using log-spaced single resonator detectors. The second and third are 20 and 30 log-spaced resonator detectors, read out in two and three respectively, to create 10 channel filterbanks. We increased the Q_r of the detectors by the appropriate factor in order to preserve R of each channel. Lastly we took the optimal backshorted detector described in the previous section and created a ten channel filterbank. We spaced the detectors so that the FWHM of one channel would coincide with neighboring detectors. The total efficiency of the sample filterbank is shown in figure 4.5a.

The individual responses of the ten-channel filterbanks are shown in figure 4.6. Across all graphs, the first

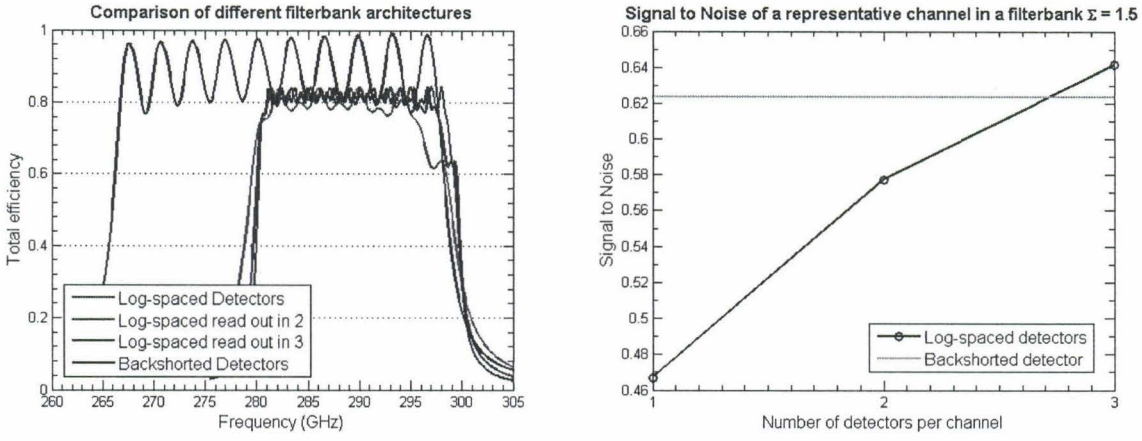

(a) (b)

Figure 4.5: Comparison between the three filterbank architectures, single log-spaced detectors, log-spaced detectors read out in three, and backshorted detectors. (a) shows the entire absorption profile. (b) shows the signal to noise of a representative channel.

channel is the highest frequency channel and has the highest response. This is because it sees uninterrupted power. In addition the last channel in the filterbank has the lowest response and a profile that differs from the rest. This is because, for the log-spaced detectors, the channel behind it reflects 25% of power in its passband. The last channel has no reflector so it's peak power is much lower.

For a log-spaced filterbank we see that we have efficiency of ~ 0.4 with a representative channel having SNR ~ 0.47. For channels with two detectors read out together, we have efficiencies of 65% with a SNR ~ 0.58. For the channels with three detectors read out together, we have efficiencies of 70% and SNR ~ 0.64. Lastly for the backshorted detectors we have efficiencies of 80% but SNR ~ 0.625. In all three cases we have lower peak performance than in the isolated case. This makes sense because channel cross talk and large wings eat up some power out of band. Both log-spaced architectures have similar SNR as their isolated case. The backshorted detector has significantly worse performance.

The backshorted detectors in our filterbank have large wings, which eat away at our signal to noise. From figure 4.6d we see that the wings are on the order of 10%. This occurs because of interchannel crosstalk. The backshort is composed of a resonator detector, and an unloaded resonator spaced $\lambda_i/4$ away. The neighboring channel's backshort is spaced $3\lambda_i/4$ away from our absorber which is a resonant wavelength and will cause strong cross talk.

We can directly see similar phenomena in our log-spaced filterbanks. If we look at figure 4.6a we also have large wings with peaks. These wings peaks coincide not with the neighboring channel, spaced $\lambda_i/2$ away, but the channel after which is spaced $3\lambda_i/4$ away. However in this case it does not kill our performance because log-spaced filterbanks only reflect 25% of power on resonance rather than 100% of power.

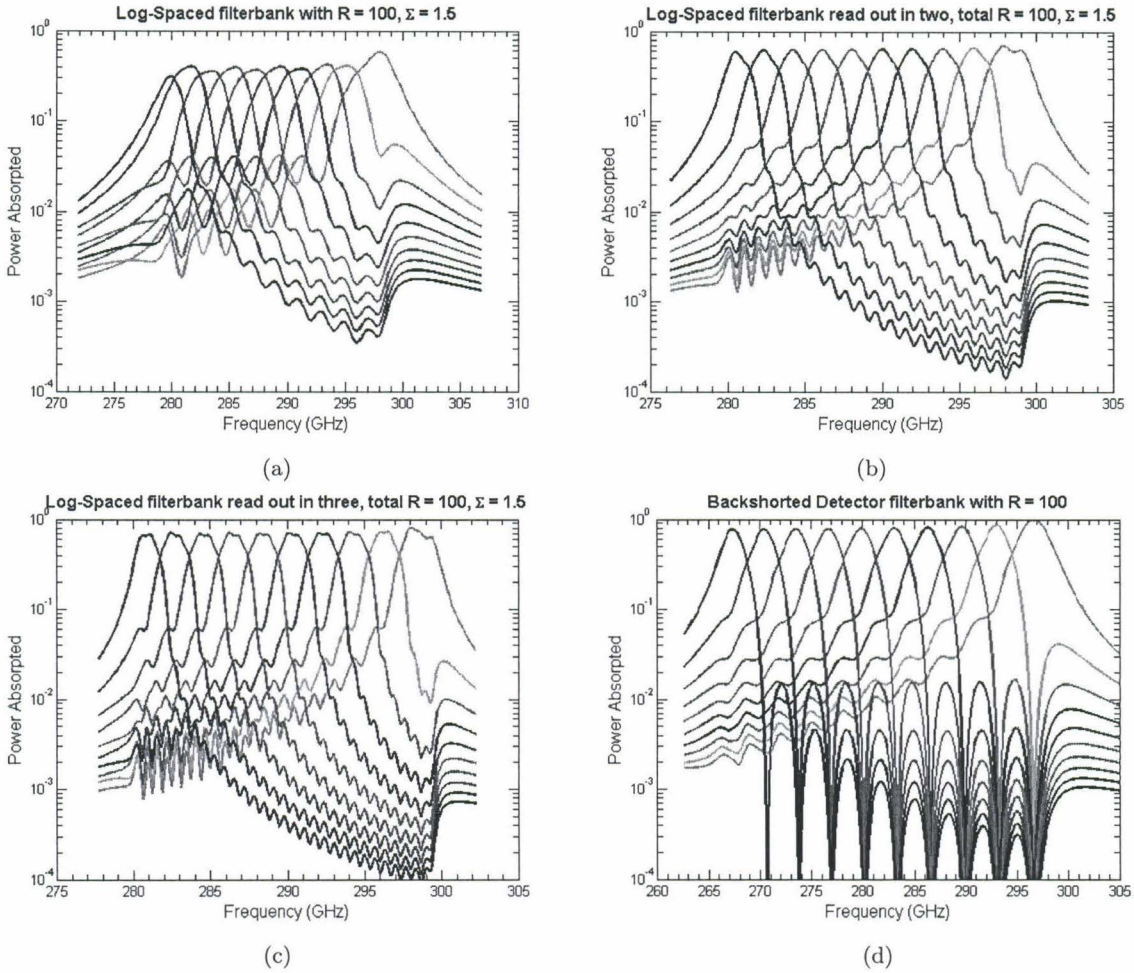

Figure 4.6: Individual channel responses for the three filterbanks shown in figure 4.5a.

4.4 Conclusion

There are several ways to improve our signal to noise. We can sum up neighboring channels in a log-spaced architecture, or through the use of a backshort.

For our log-spaced resonators read out in multiples, we have monotonic increase in SNR as we sum up channels. The approach to unity SNR is slow due to the large wings on Lorentzian profiles. We can gain higher efficiency and SNR by increasing the oversampling factor, so that each detector overlaps more in frequency. Gains plateau at around $\Sigma \sim 1.5$.

Backshorted detectors in principle can have a very high signal to noise. By detuning the backshort Q and the impedance of the absorber, we can have better than Lorentzian profiles at a small cost of sub unit efficiency. For a single isolated channel, we can get up to SNR $= 0.72$ and still get $> 90\%$ efficiency in a single detector.

In a full filterbank we can read out multiple channels or use the backshorted detector geometry. For channels composed of two resonators, the backshorted detector configuration gives the optimal SNR. For channels composed of three or more resonators, the log-spaced detectors outperforms the backshorted detector channels.

Chapter 5

Conclusion

There are several approaches to designing a better detector, however there is no single way to improve our system without affecting other aspects in our circuit. We can improve sensitivities by removing inductor volume. For $R \sim 120$ detectors, we can remove up 75% of our inductor with our given fabrication tolerances and still obtain adequate coupling. This would allow us to gain a factor of four in responsivity and therefore a factor of four in sensitivity. Because we cannot increase the size of our interdigitated capacitors, we would be forced to go to higher frequencies for our readout electronics.

Alternatively we can increase channel efficiency using backshorted detectors. This would give us a factor of two in sensitivity at the expense of increasing the length of the chip by a factor of two. In this geometry, we preserve readout frequencies.

In addition, we could combine the two approaches of higher efficiency and smaller inductors. The backshort leaves empty space which we can fill with capacitor area. We can simultaneously implement a backshort, double the capacitor area, and decrease the inductor volume by half. These changes would increase chip area by a factor of two, but preserve readout frequencies. We would get a factor of 4 in response and a factor of $\sqrt{2}$ reduction in TLS noise netting us a total $4\sqrt{2}$ improvement in sensitivity.

The performance of a spectrometer is ultimately measured by how well it detects a line. A filterbank comprised of backshorted detectors outperforms both single and double log-spaced detectors, and offers the highest signal to noise ratio for their footprint on the feedline. If we sum together three or more log-spaced detectors into a single channel, then these channels would resolve lines better than our backshorted detector filterbank. Designing a full instrument would weigh the benefits of gaining higher resolving power at the expense of each channel having a larger footprint.

Appendix A

Relating Design Parameters to Transmission Line Model

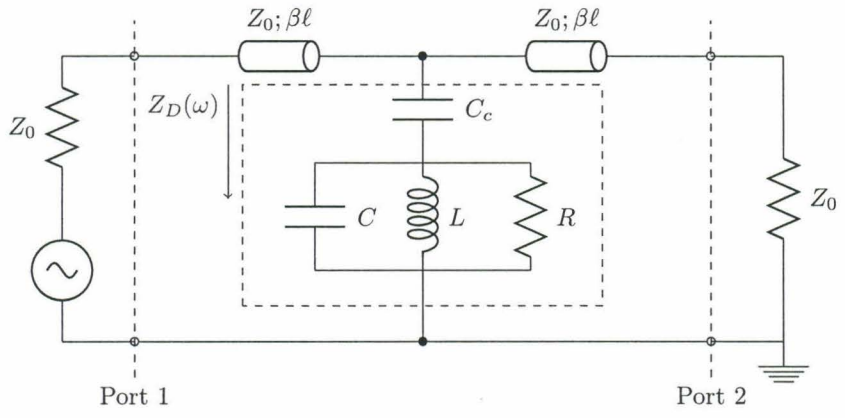

Figure A.1: Transmission line model of a single detector. We have a capacitively coupled RLC tank circuit. We want to find the equivalent $Z_D(\omega)$ which is the impedance looking down into the blue box.

When we design detectors, we typically think in terms of Q_r, Q_i and Q_c. These parameters correspond to physically measurable properties in our detector. However from an analytic standpoint, these are cumbersome to use. We want to convert these parameters into an equivalent transmission line impedance. Omid's thesis provided an analytic form for relating scatting parameters to our design parameters [12],

$$s_{21} = 1 - \frac{Q_r}{Q_c}\frac{1}{1 + 2iQ_r x} \tag{A.1}$$

$$s_{11} = s_{21} - 1 = -\frac{Q_r}{Q_c}\frac{1}{1 + 2iQ_r x} \tag{A.2}$$

s_{11} is defined as the voltage reflection coefficient. By definition, the voltage reflection coefficient is caused by an impedance mismatch between the load of the transmission line and the characteristic impedance of the line. To be complete, we can show the simplified circuit in figure A.2.

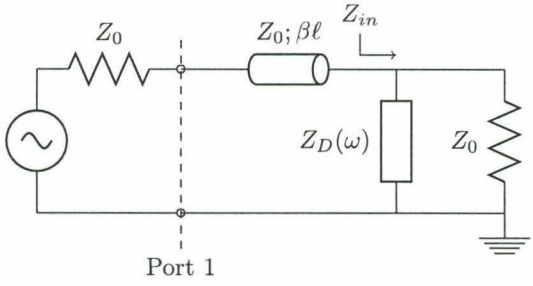

Figure A.2: Equivalent circuit to A.1. We collapsed the RLC tank circuit into $Z_D(\omega)$ and the transmission line into Z_0.

Then the reflection is simply expressed as,

$$s_{11}(\omega) = \frac{Z_{in} - Z_0}{Z_{in} + Z_0} = \frac{Z_D Z_0 - Z_0(Z_D + Z_0)}{Z_D Z_0 + Z_0(Z_D + Z_0)} = -\frac{Z_0}{2Z_D + Z_0} \tag{A.3}$$

where we used $Z_{in} = Z_D(\omega) \parallel Z_0$ is the parallel impedance of our detector and port impedance. We can invert the expression for Z_D,

$$Z_D(\omega) = -\frac{Z_0}{2}\left(1 + \frac{1}{s_{11}}\right) = \frac{Z_0}{2}\left(-1 + \frac{Q_c}{Q_r}(1 + 2iQ_r x)\right) \tag{A.4}$$

If we are on resonance, then the impedance is simply,

$$Z_D(\omega_0) = \frac{Z_0}{2}\left(\frac{Q_c}{Q_r} - 1\right) \tag{A.5}$$

In certain applications we want to specify an impedance rather than Q_r. We can invert the equation to find,

$$Q_r = \frac{Q_c}{1 + 2\frac{Z_D}{Z_0}} \tag{A.6}$$

These expressions are incredibly useful as we build up a filterbank numerically which we discuss in Appendix E and use extensively in chapter 4.

Appendix B

Matching Ports in Sonnet

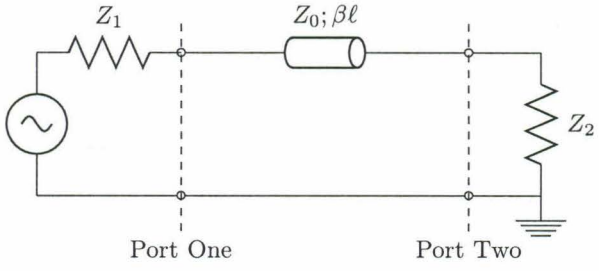

Figure B.1: Transmission line model of circuit with just a microstrip line from port 1 to port 2.

Matching ports is critical in obtaining reliable simulations. While it is possible to use semi-analytic functions to compute the microstrip impedance, they typically aren't reliable. Semi-analytic functions are extrapolated from microstrip behavior at microwave frequencies ($\sim$ 10GHz). In addition we have an inverted microstrip geometry which requires modification to what the effective dielectric would be.

It is easiest to find the microstrip impedance through simulation of a straight transmission line with arbitrary port impedances. We can fit reflection to an analytic model to find what the microstrip impedance is. The transmission line model is shown in figure B.1.

For simplicity we can set $Z_1 = Z_2 = Z_L$. The impedance from port 1 looking down the loaded transmission line is the same as equation 3.1. We repeat the equation below

$$Z_{in}(\beta\ell) = Z_0 \frac{Z_L + iZ_0 \tan(\beta\ell)}{Z_0 + iZ_L \tan(\beta\ell)} \tag{B.1}$$

Reflection at this port is simply caused by the impedance mismatch between the port and looking down the feedline,

$$s_{11} = \Gamma = \frac{Z_{in}(\beta\ell) - Z_L}{Z_{in}(\beta\ell) + Z_L} \tag{B.2}$$

Showing the explicit dependence of β on physical parameters,

$$\beta = \frac{2\pi}{\lambda} = \frac{2\pi f}{c/\sqrt{\epsilon_{\text{eff}}}} \tag{B.3}$$

where ϵ_{eff} is the effective dielectric constant for the microstrip geometry. This is different than the dielectric deposited between the ground plane and the microstrip line because field lines go through both the Si ($\epsilon_r = 11.7$) and the dielectric layer SiN ($\epsilon_r = 7$).

We have two unknowns in our system, Z_0 and ϵ_r. We can avoid doing a multiparameter fit by using Sonnet by sweeping a large frequency range capturing when reflection goes to zero. This occurs when transmission line is exactly a integer multiple of a half-wave length. When this occurs, $\beta\ell = n\pi$, and our impedance looking into a transmission line equation B.1 reduces to $Z_{in} = Z_L$. At key frequencies when the transmission line looks like half-wavelengths multiples we get exactly 0 reflection. This allows us to solve for ϵ_{eff} by setting $\beta\ell = n\pi$ and inverting the expression for ϵ_{eff}.

$$\epsilon_{\text{eff}} = \left(\frac{2\pi f^* \ell}{cn\pi}\right)^2 \tag{B.4}$$

where f^* is the frequency when we see 0 reflection, ℓ is the total length of the microstrip, n is the mode number.

Once we have solve for ϵ_{eff} we have enough information to use equation B.1 and equation B.2 to do a least-squares fit for what the characteristic impedance Z_0 should be. This allows us to match ports.

Appendix C

Kinetic Inductance in Sonnet Thick Metal Models

Sonnet is a planar EM simulation software. Metal is approximated as infinitely thin and is placed in between dielectric layers. Measurements shows that while simulation is reasonable for several key parameters, simulations underestimate coupling especially between our Nb feedline and Nb staples which are $\sim 150 - 200\mu m$ thick.

We can get more accurate simulation of coupling using Sonnet's native thick-metal model tool. Sonnet builds up thick metal by placing several thin metal layers as shown in figure C.1a. Thick films are comprised of N layers of thin film which is connected together using infinitely conductive metal vias or side walls.

While Sonnet has a thick-metal model, kinetic inductance cannot be natively incorporated in this model. By manually building up these films, we can incorporate the kinetic inductance property of thin films and apply them to thick films [17]. This capability would enable careful simulation of channel frequency and coupling between the feedline and staple.

The kinetic inductance of a film at a temperature well below T_c can be written in terms of its thickness

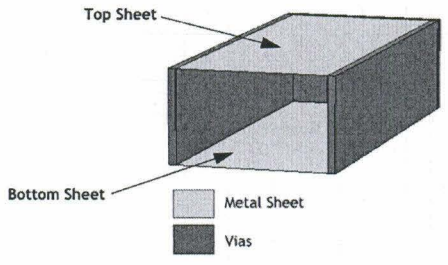

(a) Sonnet's Thick-Metal model.

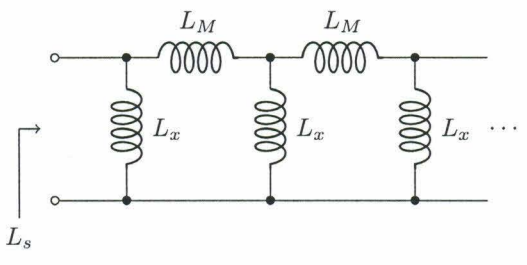

(b) Circuit model of a multi layer film.

Figure C.1: Thick metal models in Sonnet.

and London penetration depth [8],

$$L_s = \mu_0 \lambda_L \coth\left(\frac{t}{\lambda_L}\right) \tag{C.1}$$

where,

$$\lambda_L = \sqrt{\frac{m^*}{\mu n^* (e^*)^2}} \tag{C.2}$$

m^* is the effective mass of carriers, n^* is the effective density of carriers with effective charge e^*. For our niobium feedlines with $t = 200\mu m$ we have surface inductance $L_s \approx 0.13pH/sq$.

When constructing thick metal models, we want to preserve the total inductance of our film. Each film has its inherent kinetic inductance term and an additional mutual inductance between the sheets. The equivalent circuit model shown in figure C.1b. We can find the mutual inductance L_M by looking a a parallel plate. Suppose we had a surface current flowing through the plates with $J_s = I/w$. The application of Ampere's law gives us a magnetic field parallel to the plate $B = \mu_0 I$. The magnetic flux through the parallel plate is $\Phi = B \cdot h = \mu_0 I h$ which gives us an inductance,

$$L_M = \frac{\Phi}{I} = \mu_0 h = \mu_0 \frac{t}{N-1} \tag{C.3}$$

where we converted the height of the parallel plate separation h into total film thickness divided by the number of sheets $h = t/(N-1)$. If we specify the height of our Nb and the number of sheets, and the total surface inductance L_s, we have enough information to solve the circuit shown in figure C.1b.

We simulated an unloaded resonator to observe the effects of placing several layers. We increased the dielectric thickness of the SiN in order to preserve the $0.5\mu m$ thickness between the ground plane and the microstrip line. The table of inductances is given in table C.1 and simulation results as shown in figure C.2. Adding additional sheets causes increased coupling. This decreases both the fitted Q_r of the channel and shifts the center frequency of the channel. Care must be taken when doing this simulation because adding sheets causes a small change in the characteristic impedance of our transmission line and would require a re-optimization of ports.

Number Sheets	$L_M(pH)$	$L_s(pH)$
1	–	0.13
2	1.9×10^{-4}	0.26
3	9.4×10^{-5}	0.39
4	6.3×10^{-5}	0.52
5	4.7×10^{-5}	0.65

Table C.1: Table showing the sheet inductances as we increase the number of sheets from 1 to 5 to model thick niobium.

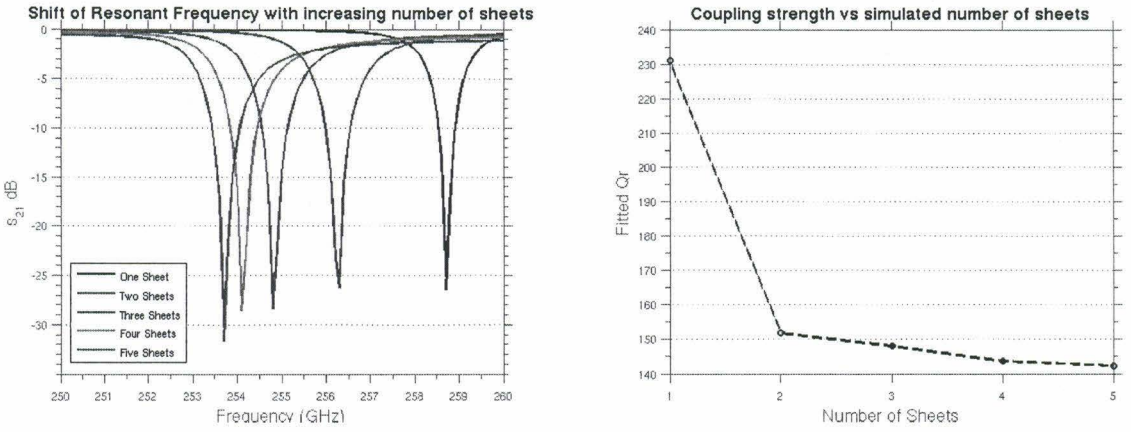

(a) (b)

Figure C.2: Resonant profiles and fitted Q_r as we increase the number of sheets in our simulation. Increased coupling causes an increase in coupling capacitance resulting in shifts in both the resonant frequency and decreased Qs.

Appendix D

Obtaining current density from Sonnet simulations

Sonnet can solve for the current densities on the surface of conductive surfaces. It has a native current density viewer which allows us to generate colormaps of currents to gain an intuitive understanding of the lithographed circuit behavior.

In principle this information can be exported into the csv file and analyzed separately. This data can be imported as a large matrix which the position in the matrix corresponds to a physical location in the circuit. The current density would give information on where power is being deposited in our system. In our filterbank simulations, we could back out how power is being distributed to all the detectors and observe cross-talk between the channels.

In practice finding the current density at all frequencies of interest is a painful process. For each geometry we would have to cut out the regions of interest for each detector.

SonnetLab is a Matlab toolbox and acts as a wrapper around Sonnet. SonnetLab with Matlab creates one smooth continuous workflow. SonnetLab creates geometries and analyzes them while Matlab is a powerful tool for data analysis and automation.

SonnetLabs gives us the ability to analyze where power is being deposited in our filterbank at what frequencies to find the response function of each channel in a complex, interacting filterbank. Below is pseudocode in implementing this technique

(a) The sonnet file is simply imported calling the function

```
Project = SonnetProject(filename)
```

(b) Geometry objects in Sonnet are stored as polygon objects. We can retrieve a list of these polygons using the following function

```
listpoly_IDS = Project.getAllPolygonIds();
```

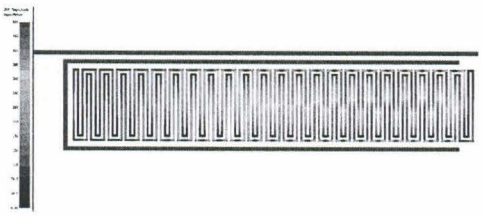

(a) Sonnet's native current density viewer.

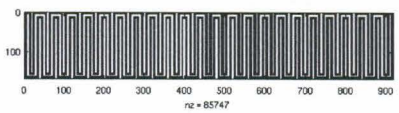

(b) Importing currents into Matlab and showing nonzero elements of the matrix.

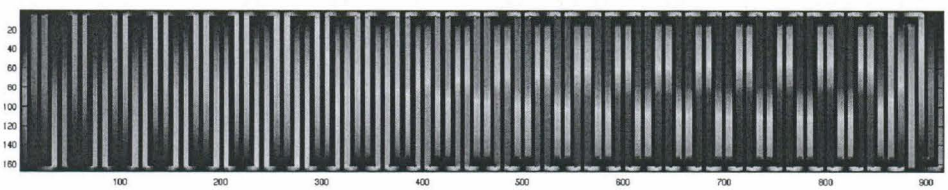

(c) Power absorbed.

Figure D.1: Figure showing the workflow. Currents are simulated in Sonnet as shown in figure D.1a. The current density file is imported into Matlab and the region of interest is cut out D.1b.

(c) We want to loop through the polygon list to identify which polygons correspond to the detector material.

```
polygon_num = Project.findPolygonUsingId(id); %Get the polygon number from
    the polygon ID.
polygon = Project.getPolygon(polygon_num); %Obtain the polygon object
metalType = polygon.MetalType; %The metalType returns 0,1,... where the
    number is the metal index in metaltypes.
%Append the polygon to the list if it matches the correct metal type (1 =
    TiN in our case)
if metalType == 1
        inductor_list(end + 1) = polygon
end
```

(d) Define the simulation parameters

```
%Define port parameters. JXYPort(Port Num, Voltage, Phase, Resistance =
    32.9, Reactance = 0, Inductance = 0, Capacitance = 0). 32.9Ohms is the
    characteristic impedance of our 1um wide inverted microstrip lines at
    our frequencies of interest.
```

```
Port1 = JXYPort(1,1,0,32.9,0,0,0);
Port2 = JXYPort(2,0,0,32.9,0,0,0);
%Grab current data
%exportCurrents(Region, Type (JX,JY,JXY), Ports, Frequency, XGrid
    Resolution, YGrid Resolution, Metal Layer). If Region = [], then the
    method returns current density for the whole layout.
resol  = 0.1; %Cell size resolution in microns
Data = Project.exportCurrents([], 'JXY',[Port1 Port2], freq, resol, resol,
    0);
```

(e) We want to define the regions of interest. We loop through all the detectors in our project file and grab the bounding region.

```
%Grab the coordinates for detector
inductor = inductor_list(index);
startX = inductor.BoundingBox.Start.X;
startY = inductor.BoundingBox.Start.Y;
endX = inductor.BoundingBox.End.X;
endY = inductor.BoundingBox.End.Y;
%Convert the coordinates of the detector to matrix indices (i,j) of
    currents
elem_per_length = 1/resol;
leftX = startX*elem_per_length ;
rightX = endX*elem_per_length;
topY = startY*elem_per_length;
botY = endY*elem_per_length;
```

(f) We can grab the current data, which has units of A/m and then find the power dissipated.

```
%Make a matrix of the data we want. Each element (i,j) corresponds to the
    JXY current density for the cell (i,j). Note that the matrix element
    (100,100) corresponds to (10um,10um) on the actual circuit because of
    resolution.
matrix_currents = Data.Data(topY:botY, leftX:rightX);
```

```
sparse_currents = sparse(matrix_currents);%Remove all the nonzeros for
    speed

diff_elem = resol*10^(-6); %Converts um units to meters
z0 = 50; %The sheet resistance of the material
%Power dissipated is the sum of I^2 R.
total_pow = sum(nonzeros(sparse_currents).^2*diff_elem.^2*z0);
```

(g) Loop through steps (e) and (f) to grab power from all detectors.

Appendix E

Numerical analysis of filterbank circuits

E.1 ABCD Parameters for filterbank elements

Full filterbanks are complex circuits. Channels inherently interact through the main feedline so single channel simulations is not sufficient to understanding their performance. It is critical to understand how channels behave in order to optimize filterbank performance.

Many channel filterbanks are computational expensive to analyze using EM simulation tools such as Sonnet or HFSS. For a one channel filterbank, Sonnet takes $\sim$ 3 minutes to analyze a single channel. For a ten-channel filterbank Sonnet takes roughly $\sim$ 2 hours. In order to perform the current analysis for the same system, it would take an additional $\sim$ 30 hours. Sonnet simulations is not the right approach to solving large filterbanks.

We can model our filterbank as a transmission line model. Each resonator/detector can be modeled as a RLC tank circuit. We place transmission lines between each of the detectors. The full filterbank performance can be solved by stringing together ABCD matrices. From Pozar, the conversion between s-parameters to ABCD parameters is given by,

$$A = \frac{(1+s_{11})(1-s_{22})+s_{12}s_{21}}{2s_{21}} \tag{E.1}$$

$$B = Z_0\frac{(1+s_{11})(1+s_{22})-s_{12}s_{21}}{2s_{21}} \tag{E.2}$$

$$C = \frac{1}{Z_0}\frac{(1-s_{11})(1-s_{22})-s_{12}s_{21}}{2s_{21}} \tag{E.3}$$

$$D = \frac{(1-s_{11})(1+s_{22})+s_{12}s_{21}}{2s_{21}} \tag{E.4}$$

Because we have a symmetric system as shown in figure (figure in chapter 3), our s-parameters $s_{11} = s_{22}$

and $s_{21} = s_{12}$. Recall from the analysis in chapter 3 that we argued $s_{21} = 1 + s_{11}$. Recall that the forward transmission is,

$$s_{21} = 1 - \frac{Q_r}{Q_c}\frac{1}{1 + 2iQ_r x} \tag{E.5}$$

which gives us enough information to find the ABCD matrix for our resonator, expressed in terms of variable parameters Q_i, Q_c,

$$\text{ABCD}_{\text{tline}} = \begin{pmatrix} 1 & 0 \\ \frac{2}{Z_0}\left(-1 + \frac{1}{s_{21}}\right) & 1 \end{pmatrix} = \begin{pmatrix} 1 & 0 \\ \frac{2}{Z_0}\frac{Q_c}{Q_r}(1 + 2iQ_r x) & 1 \end{pmatrix} \tag{E.6}$$

While the ABCD matrix of a general transmission line is,

$$\text{ABCD}_{\text{tline}} = \begin{pmatrix} \cos(\beta\ell) & iZ_0 \sin(\beta\ell) \\ \frac{i}{Z_0}\sin(\beta\ell) & \cos(\beta\ell) \end{pmatrix} \tag{E.7}$$

where β is the wavenumber $\beta = \frac{2\pi}{\lambda} = 2\pi\sqrt{\epsilon_r} f/c$ and ℓ is the length of the transmission line. Simply by stringing together these parameters, and inverting back to scattering parameters, we recover the response of the filterbank.

E.2 Solving full filterbank

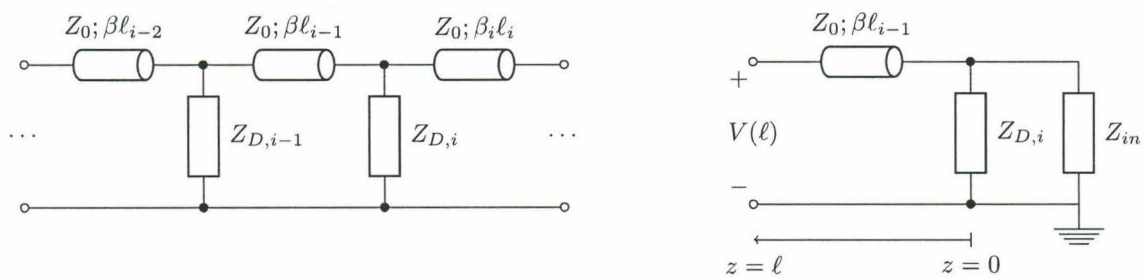

Figure E.1: On the left, we have a transmission line model of our filterbank circuit where $Z_{D,i}$ is the impedance of detector i. On the right we show the analysis for a single detector. We simplify the problem to a loaded transmission line with $Z_L = Z_D(\omega) \parallel Z_{in}$, where Z_{in} is the impedance looking down the transmission line to the right at that node.

The process is more involved in order to compute the response of each individual detector within the filterbank. We can model the system for each individual detector as a terminated, lossless transmission line problem. We can find the power deposited in each detector by finding the voltage at each node.

The general filterbank can be modeled as figure E.1 with the model at a particular detector is simply

a loaded transmission line problem simplified in figure E.1b. We define the node of the detector to be at $z = 0$. The impedance looking to the right is simply the impedance looking down a loaded transmission line given in equation 3.1.

The voltage at any point in the transmission line is sum of the forward and backwards propagating wave coming from $z > 0$,

$$V(z) = V_0^+ e^{-i\beta z} + V_0^- e^{i\beta z} \tag{E.8}$$

which we can simplify using the voltage reflection coefficient, referencing the circuit in figure E.1 to write that the load impedance is the parallel impedance of the detector in the input impedance.

$$\Gamma = \frac{V_0^-}{V_+^0} = \frac{Z_L - Z_0}{Z_L + Z_0} = \frac{Z_D(\omega) \parallel Z_{in} - Z_0}{Z_D(\omega) \parallel Z_{in} + Z_0} \tag{E.9}$$

so that equation E.8 simplifies to,

$$V(z) = V_0^+ (e^{-i\beta z} + \Gamma e^{i\beta z}) \tag{E.10}$$

We want to find the voltage at the detector,

$$V(0) = V_0^+ (1 + \Gamma) \tag{E.11}$$

and the voltage at the input,

$$V(\ell) = V_0^+ (\exp^{-i\beta\ell} + i\Gamma \exp^{i\beta\ell}) = iV_0^+ (e^{-i\frac{\pi}{2}\frac{f}{f_{0,i-1}}} + \Gamma e^{i\frac{\pi}{2}\frac{f}{f_{0,i-1}}}) \tag{E.12}$$

In the last step we used the fact that $\beta = \frac{2\pi f\sqrt{\epsilon_r}}{c}$, and $\ell_i = \frac{c}{4\sqrt{\epsilon_r}}\frac{1}{f_{0,i}}$ where $f_{0,i}$ is the center frequency of the i^th resonator. Using both equation E.11 and equation E.12 we can relate the voltage at the detector $V(0)$ to the voltage at the input $V(\ell)$.

$$V(0) = V(\ell)\frac{1 + \Gamma}{e^{-i\frac{\pi}{2}\frac{f}{f_{0,i-1}}} + \Gamma e^{i\frac{\pi}{2}\frac{f}{f_{0,i-1}}}} \tag{E.13}$$

Voltage and current are related to complex power by $S = \frac{1}{2}V^* I$. $1/2$ is required because we are looking at amplitudes V, I rather than the root-mean-squared (rms) amplitude. Complex power is broken down into a real and imaginary term $S = P + iQ$ where physically P is the real power dissipated and Q is the reactive power which oscillates around our circuit but is not absorbed. Power dissipated by a detector is then given

$$P = \frac{1}{2}\mathrm{Re}\{V^*(0)I(0)\} = \frac{1}{2}\mathrm{Re}\left\{\frac{V_0^2}{Z_D}\right\} \tag{E.14}$$

where $Z_D(\omega)$ is the impedance looking into our detector. In general it is complex and a function of frequency. We can relate this to our design parameters Q_r, Q_c from appendix A.

E.3 Implementation in Matlab

We can implement this in Matlab to completely solve our circuit at any given frequency.

(i) We first define a Resonator object which has parameters Q_r, Q_c, f_0 with appropriate getters/setters. We can define a method that gives us $s_{21}(\omega), s_{11}(\omega)$ and the equivalent ABCD parameters at a given frequency

(ii) We create a filterbank by defining a cell array composed of Resonator objects.

(iii) We want to find the input impedance Z_{in} looking down the transmission line to the right of each resonator i.

  (a) String together the transmission line elements' ABCD parameters to the right of resonator i.

  (b) Invert to scattering parameters.

  (c) Solve for Z_{in} by relating $s_{11} = \Gamma = \frac{Z_{in}-Z_0}{Z_{in}+Z_0}$.

  The problem is most efficiently solved if we work backwards; we begin at the end of the circuit at port 2 and string together the ABCD parameters of elements as we work our way to the front of the circuit.

(iv) We want the voltage at the node of each resonator. We solve the problem forwards starting at port one beginning with $V(\ell) = 1$. We use equation E.13 to propagate the voltage to each node down the transmission line.

(v) Now that we have both an array of voltages at each detector V_i and the impedance of each detector $Z_{D,i}$, we can find the power dissipated in the detector according to equation E.14.

This method is general and can scale to arbitrary large filterbanks. By implementing this in Matlab, we can find the transmission and reflection of a ten channel filterbank on the order of 2 seconds. This rapid improvement in speed not only allows us to simulate larger and more complex filterbanks, but aids in gaining intuition of how the channels electrically interact with one another through the feedline.

We compare a Sonnet simulation of a complex filterbank with this numerical method. The filterbank is comprised of 10 resonators, with half of them unloaded, to make a resonant backshort filterbank. The Q_r, Q_c were found by isolating each staple in the filterbank and shown in table E.1. We compare Sonnet

	Q_r	Q_c	$f_0(GHz)$
Resonator 1	90.8	293.3	209.4
Resonator 1 Short	133.2	133.2	209.4
Resonator 2	91.0	293.4	207.8
Resonator 2 Short	133.1	133.1	207.7
Resonator 3	91.3	294.1	206.3
Resonator 3 Short	133.2	133.2	206.2
Resonator 4	90.9	290.7	204.8
Resonator 4 Short	132.9	132.9	204.7
Resonator 5	92.7	293.5	203.3
Resonator 5 Short	133.4	133.4	203.3

Table E.1: Table showing the design of a 5-backshort paired channels. These values were obtained from simulating each resonator independently in Sonnet and fitting the $s_{21}(\omega)$ results to the standard isolated resonator.

simulations with our numerical results shown in figure E.2. As we can see we have both fairly reasonable agreement between our numerical results and Sonnet simulations of the overall profile in figure E.2a. We have good agreement for the power dissipated in each channel, shown in figure E.2b. The transmission line model captures the channel to channel interaction as evidence by the large wings of the resonator response.

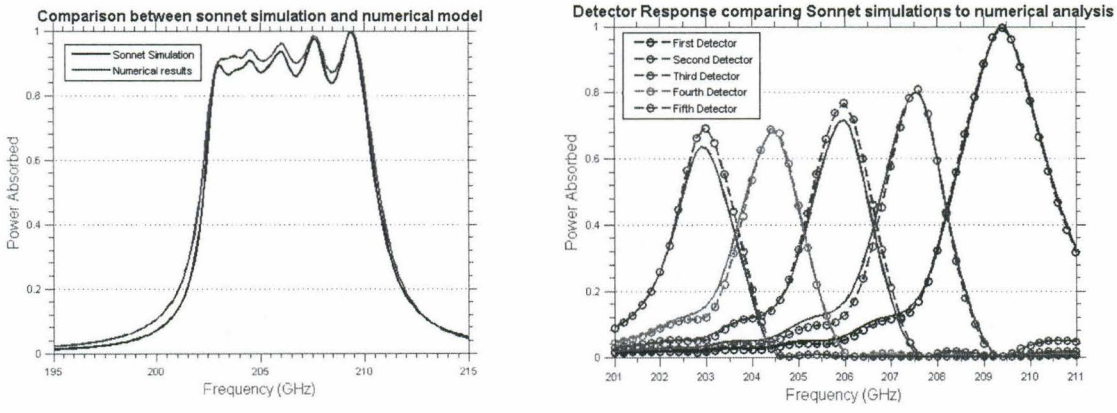

(a) (b)

Figure E.2: Comparision between the current model through Sonnet in section ?? and the numerical analysis described above in this section.

Bibliography

[1] P. S. Barry, E. Shirokoff, A. Kovács, T. J. Reck, S. Hailey-Dunsheath, C. M. McKenney, L. J. Swenson, M. I. Hollister, H. G. Leduc, S. Doyle, R. O'Brient, N. Llombart, D. Marrone, G. Chattopadhyay, P. K. Day, S. Padin, C. M. Bradford, P. D. Mauskopf, and J. Zmuidzinas. Electromagnetic design for SuperSpec: a lithographically-patterned millimetre-wave spectrograph. In *Society of Photo-Optical Instrumentation Engineers (SPIE) Conference Series*, volume 8452 of *Society of Photo-Optical Instrumentation Engineers (SPIE) Conference Series*, page 2, September 2012.

[2] W. Bogaerts, P. De Heyn, T. Van Vaerenbergh, K. De Vos, S. Kumar Selvaraja, T. Claes, P. Dumon, P. Bienstman, D. Van Thourhout, and R. Baets. Silicon microring resonators. *Laser & Photonics Reviews*, 6(1):47–73, 2012.

[3] P. K. Day, H. G. LeDuc, B. A. Mazin, A. Vayonakis, and J. Zmuidzinas. A broadband superconducting detector suitable for use in large arrays. *Nature*, 425:817–821, October 2003.

[4] Jiansong Gao. *The Physics of Superconducting Microwave Resonators.* PhD thesis, California Institute of Technology, May 2008.

[5] Y. Gong, A. Cooray, M. Silva, M. G. Santos, J. Bock, C. M. Bradford, and M. Zemcov. Intensity Mapping of the [C II] Fine Structure Line during the Epoch of Reionization. *The Astrophysical Journal*, 745:49, January 2012.

[6] David Griffiths. *Introduction to Electrodynamics, 3rd ed.* Pearson Benjamin Cummings, San Francisco, 2008.

[7] Steve Hailey-Dunsheath. Superspec NEP Scaling, and Predicted Gen-4 Sensitivity, August 2014.

[8] A. R. Kerr. Surface Impedance of Superconductors and Normal Conductors in EM Simulators, August 1999.

[9] A. Kovacs and J. Zmuidzinas. Transmission-Line Resonator Spectrometers. Internal Memo, December 2010.

[10] H. G. Leduc, B. Bumble, P. K. Day, B. H. Eom, J. Gao, S. Golwala, B. A. Mazin, S. McHugh, A. Merrill, D. C. Moore, O. Noroozian, A. D. Turner, and J. Zmuidzinas. Titanium nitride films for ultrasensitive microresonator detectors. *Applied Physics Letters*, 97(10):102509, September 2010.

[11] D. C. Mattis and J. Bardeen. Theory of the Anomalous Skin Effect in Normal and Superconducting Metals. *Physical Review Letters*, 111:412, 1958.

[12] Omid Noorzian. *Superconducting microwave resonator arrays for submillimeter/far-infrared imaging.* PhD thesis, California Institute of Technology, July 2012.

[13] David M. Pozar. *Microwave Engineering, 4th ed.* John Wiley & Sons, Inc., Singapore, 2012.

[14] Dominik G. Rabus. *Integrated Ring Resonators.* Springer Berlin Heidelberg, 2007.

[15] P. S. Barry C. M. Bradford G. Chattopadhyay P. Day S. Doyle M. Hollister A. Kovacs H. G. LeDuc P. Mauskopf C. M. McKenney R. Monroe R. O'Brient S. Padin T. Reck L. Swenson C. E. Tucker J. Zmuidzinas S. Hailey-Dunsheath, E. Shirokoff. In *Society of Photo-Optical Instrumentation Engineers (SPIE) Conference Series), Month = Aug, Title = Status of SuperSpec: a broadband, on-chip millimeter-wave spectrometer, Volume = 9153, Year = 2014, Bdsk-Url-1 = http://dx.doi.org/10.1117/12.2057229.*

[16] E. Shirokoff, P.S. Barry, C.M. Bradford, G. Chattopadhyay, P. Day, S. Doyle, S. Hailey-Dunsheath, M.I. Hollister, A. Kovács, H.G. Leduc, C.M. McKenney, P. Mauskopf, H.T. Nguyen, R. O'Brient, S. Padin, T.J. Reck, L.J. Swenson, C.E. Tucker, and J. Zmuidzinas. Design and Performance of SuperSpec: An On-Chip, KID-Based, mm-Wavelength Spectrometer. *Journal of Low Temperature Physics*, pages 1–6, 2014.

[17] A. Vayonakis, H. G. LeDuc, C. Luo, and J. Zmuidzinas. Precision Measurements of the Millimeter-Wave Properties of Superconducting Thin-Film Microstrip Lines, 2003.

[18] Jonas Zmuidzinas. Superconducting Microresonators: Physics and Applications. *Annual Review of Condensed Matter Physics*, 3(1):169–214, 2012.